A first glimpse at the influence of body mass in the morphological integration of the limb long bones: an investigation in modern rhinoceroses

Christophe Mallet, Guillaume Billet, Alexandra Houssaye, Raphael Cornette

A first glimpse at the influence of body mass in the morphological integration of the limb long bones: an investigation in modern rhinoceroses

Christophe Mallet[1], Guillaume Billet[2], Alexandra Houssaye[1], Raphaël Cornette[3]

1 Mécanismes adaptatifs et évolution (MECADEV), UMR 7179, MNHN, CNRS, 55 rue Buffon, CP 55, 75005, Paris, France

2 Centre de Recherche en Paléontologie – Paris (CR2P), UMR CNRS 7207, MNHN, CNRS, SU, 8 rue Buffon, CP 38, 75005 Paris, France

3 Institut de Systématique, Evolution, Biodiversité (ISYEB), UMR 7205, MNHN, CNRS, SU, EPHE, UA, 57 rue Cuvier, CP 50, 75005 Paris, France

Corresponding author:

Christophe Mallet

55 rue Buffon, CP 55, 75005, Paris, France

Email address: christophe.mallet@edu.mnhn.fr

Abstract

The appendicular skeleton of tetrapods is a particularly integrated structure due to the shared developmental origin or similar functional constraints exerted on its elements. Among these constraints, body mass is considered as strongly influencing its integration but its effect on shape covariation has rarely been addressed in mammals, especially in heavy taxa. Here we propose to explore the covariation patterns of the long bones in heavy animals and their link to body mass. We investigate the five modern rhinoceros species, which display an important range of body weight. We used a 3D geometric morphometric approach to describe the shape covariation of the six bones composing the stylopodium and zeugopodium both among and within species. Our results indicate that the appendicular skeleton of modern rhinos is a strongly integrated structure. At the interspecific level, the shape covariation is roughly similar between all pairs of bones and mainly concerns the muscular insertions related to powerful flexion and extension movements. The forelimb integration appears higher and more related to body mass than that of the hind limb, suggesting a specialization for weight support. The integration of the stylopodium elements does not seem to relate to body mass in our sample, which suggests a higher effect of shared developmental factors. Conversely, the covariation of the zeugopodium bones seems more associated with body mass, particularly for the radius-ulna pair. The fibula appears poorly integrated with other bones, especially within non-*Rhinoceros* species, which may represent a case of parcellation due to a functional dissociation between the hind limb bones. The exploration of the integration patterns at the intraspecific level also highlights a more prominent effect of age over individual body mass on shape covariation within *C. simum*. This study lends support to previous hypotheses indicating a link between high body mass and high integration level, highlighting that one single constraint – body mass – can lead to different covariation patterns even between closely-related taxa.

Keywords

Rhinocerotidae; geometric morphometrics; functional morphology; appendicular skeleton; locomotion; morphological integration; body mass

Introduction

The morphology of the different anatomical parts constituting organisms are known to be influenced by interactions between these parts due to shared developmental origin, phylogenetic legacy, functional constraints or structural requirements (Olson & Miller 1958; Van Valen 1965; Cheverud 1982; Gould 2002; Hallgrímsson et al. 2002; Cubo 2004; Goswami & Polly 2010; Goswami et al. 2014). The tendency of morphological traits to covary under the influence of these factors is known as morphological integration (Olson & Miller 1958; Van Valen 1965). These factors can indeed increase morphological integration of the whole body or parts of it, but they can also act locally to produce stronger covariation within parts than with other units (e.g. modules – Hallgrímsson et al. 2002; Young & Hallgrímsson 2005; Klingenberg 2008; Goswami et al. 2014). Morphological integration is therefore classically explored through the study of covariation between sets of linear measurements or shape data (Van Valen 1965; Klingenberg 2008; Goswami & Polly 2010; Bookstein 2015).

Among tetrapods, the appendicular skeleton is a particularly integrated structure due to the common developmental origin of its parts (serial homology – Young & Hallgrímsson 2005; Bininda-Emonds et al. 2007; Sears et al. 2015) and shared functional constraints linked to locomotion and ecology (Hallgrímsson et al. 2002; Young & Hallgrímsson 2005; Goswami et al. 2014; Martín-Serra et al. 2015; Botton-Divet et al. 2018). In this framework, it has been hypothesized that the functional specialization of the appendicular skeleton is associated with a decrease of the integration level between limbs and serially homologous elements, and an increase of the within-limb integration (Hallgrímsson et al. 2002; Young & Hallgrímsson 2005). This has been particularly observed for some extreme locomotor adaptations like flight in bats or bipedal locomotion in hominoids, which led to a strong specialization of a specific part of the appendicular skeleton and consequently to a decrease of the general integration (Young & Hallgrímsson 2005; Young et al. 2010; Bell et al. 2011). Moreover, among quadrupedal mammals, the loss of the clavicle allows a greater mobility of the scapula, playing an active role in locomotion (Gasc 2001; Schmidt & Fischer 2009). This led to a shift in the functional relations between limb parts, where the serially homologous elements are not functionally analogous anymore (Gasc 2001; Schmidt & Fischer 2009) (Figure 1). At the interspecific level (e.g. evolutionary integration – Klingenberg 2014), it has been shown that many terrestrial taxa (equids, carnivorans, marsupials) present a strong general integration among all their limb long bones (Bennett & Goswami 2011; Kelly & Sears 2011; Fabre et al. 2014; Martín-Serra et al. 2015; Hanot et al. 2017, 2018, 2019; Botton-Divet et al. 2018; Martín-Serra & Benson 2019), with a covariation mainly linked to the locomotion and shared phylogenetic history. But few studies explored the patterns of morphological integration of the appendicular skeleton among mammals at the intraspecific level (e.g. static or developmental integration – Klingenberg 2014) and tempted to

compare them with the patterns observed at the interspecific level (Young et al. 2010; Hanot et al. 2017, 2018, 2019).

The support of a heavy mass is likely an important factor influencing the shape and integration of the appendicular skeleton. Among mammals, many lineages displayed an increase of their body mass along their evolutionary history (Depéret 1907; Raia et al. 2012; Baker et al. 2015; Bokma et al. 2016). Biomechanical studies indicate that the shape of the limb bones should be driven by stress linked to mass support during the stance and the displacement of the animal (Hildebrand 1974; Biewener 1983, 1989a,b). However, few studies have explored the precise role exerted by body mass on the shape variation of the limb bones (Biewener 1983; Bertram & Biewener 1992; Fabre et al. 2013; Mallet et al. 2019). Likewise, the influence of body mass on integration patterns among limb bones is poorly known. Previous studies on relatively light taxa indicated a limited effect of body mass on integration patterns, overcome by other factors such as locomotor ecology (Martín-Serra et al. 2015; Botton-Divet et al. 2018; Martín-Serra & Benson 2019). At the opposite, other works proposed that body mass may still have an impact on the shape covariation of the limb long bones (Hanot et al. 2017; Randau & Goswami 2018), possibly more pronounced for heavier species (Schmidt & Fischer 2009). Drawing on this, we chose to explore the integration patterns among modern rhinoceroses, constituting the second heaviest terrestrial group after elephants among modern mammals (Alexander & Pond 1992). Whereas body size and mass poorly vary among the three species of elephants, the five modern species of rhinos surviving nowadays display a wide range of body mass (BM): *Dicerorhinus sumatrensis* (Fischer, 1814) – mean BM: 775 kg; *Diceros bicornis* (Linnaeus, 1758) – mean BM: 1,050 kg; *Rhinoceros sondaicus* Desmarest, 1822 – mean BM: 1,350 kg; *Rhinoceros unicornis* Linnaeus, 1758 – mean BM: 2,000 kg; and *Ceratotherium simum* (Burchell, 1817) – mean BM: 2,300 kg (Dinerstein 2011). This range of body mass can be highly variable within each species due to sexual dimorphism or between wild and captive specimens: 600 – 950 kg for *Ds. sumatrensis*; 800 – 1,300 kg for *Dc. bicornis*; 1,200 – 1,500 kg for *R. sondaicus*; 1,270 – 2,800 kg for *R. unicornis*; 1,350 – 3,500 kg for C. *simum* (Zschokke & Baur 2002; Dinerstein 2011). *Ceratotherium simum* and *Dc. bicornis* are present in Africa while the three other species only live in Asia. While a few studies have explored the shape variation of their long bones in relation to the ecology, phylogeny and functional constraints, such as body mass (Guérin 1980; Eisenmann & Guérin 1984; Mallet et al. 2019), no work has focused on the integration of their appendicular skeleton and its relationship to these factors. The aim of this study is thus to explore shape covariation patterns among limb long bones within and between species in order to highlight potential influence of body mass.

Here we propose to investigate the integration patterns of the shape of the limb long bones among the five species of modern rhinos, to quantify the integration level within and between limbs and to explore whether body mass could influence covariation patterns. In order to describe precisely the shape covariations by taking into consideration the whole shape of the bones in three dimensions, our analyses were done using 3D geometric morphometrics. They were performed at both interspecific and intraspecific levels, taking phylogenetic relationships into account where necessary. Although phylogeny is still debated among rhinos, notably regarding the position of *Ds. sumatrensis*, the monophyly of the African rhinos (*Ceratotherium* and *Diceros*) and the one of *Rhinoceros* species are considered as consensual (Antoine 2002; Willerslev et al. 2009; Gaudry 2017; Cappellini et al. 2019). In accordance with previous works, we hypothesize that the shape of limb long bones among rhinos should be: 1) strongly integrated as in other quadrupedal mammals at both interspecific and intraspecific levels (Hanot et al. 2017); 2) relatively homogenous between fore- and hind limbs as in other quadrupedal mammals (Martín-Serra et al. 2015; Hanot et al. 2017); 3) more strongly integrated than in lighter mammal species (Schmidt & Fischer 2009); 4) showing similar patterns of shape covariation at both interspecific and intraspecific levels (Klingenberg 2014). This will allow us to emphasize how body mass could influence the structure of the limb long bones among rhinos.

Material and Methods

Studied sample

The dataset was composed of 50 complete skeletons housed in different European and American museums and belonging to the five extant rhino species: *Ceratotherium simum* (15 specimens), *Dicerorhinus sumatrensis* (9 specimens), *Diceros bicornis* (10 specimens), *Rhinoceros sondaicus* (7 specimens) and *Rhinoceros unicornis* (9 specimens) (Table 1). We considered individuals with fully fused epiphyses (adults) or individuals where the line of the epiphyseal plates was still visible on some bones (subadults). Bones with breakages or unnatural deformations were not selected. The sample involved males, females and specimens without sex information, as well as captive and wild specimens. All anatomical terms follow classic anatomical and veterinary works (Guérin 1980; Federative Committee on Anatomical Terminology 1998; Antoine 2002; Barone 2010) and are given in Supplementary Figure S1.

3D models

Most of the bones were digitized using a structured-light three-dimensional scanner (Artec Eva) and reconstructed with Artec Studio Professional software (v12.1.1.12—Artec 3D, 2018). Twelve bones were digitized with a photogrammetric approach, following Mallison & Wings (2014) and Fau, Cornette & Houssaye (2016). Sets of photos were used to reconstruct 3D models using Agisoft Photoscan software (v1.4.2—Agisoft, 2018). Each mesh was decimated to reach 250,000 vertices and 500,000 faces using MeshLab software (v2016.12—Cignoni et al., 2008). Only left bones were selected for digitization; when left sides were not available, right bones were selected instead and mirrored before analysis.

3D geometric morphometrics

The shape covariation was analysed using a 3D geometric morphometrics approach. This widely-used methodology allows to quantify the morphological differences between objects by comparing the spatial coordinates of points called landmarks (Adams et al. 2004; Zelditch et al. 2012). This method can also be easily extended to the study of shape covariation (Goswami & Polly 2010; Bardua et al. 2019). Bone shape was quantified by placing a set of anatomical landmarks and curve and surface sliding semi-landmarks on the meshes, following Gunz & Mitteroecker (2013), Botton-Divet et al. (2016) and Mallet et al. (2019). We placed all landmarks and curves using the IDAV Landmark software (v3.0—Wiley et al., 2005). We created a template to place surface semi-landmarks for each bone. We used the same number and position for anatomical landmarks and curve sliding semi-landmarks than in the protocol described in Mallet et al. (2019) but the number of surface sliding

semi-landmarks was reduced for all the bones – except the fibula – to improve the computation duration (see Supplementary Information Data S2). The specimen *C. simum* RMCA 1985.32-M-0001 was arbitrarily chosen to be the initial specimen on which all anatomical landmarks, curve and surface sliding semi-landmarks were placed. This specimen was then used as a template for the projection of surface sliding semi-landmarks on the surface of all other specimens. Projection was followed by a relaxation step to ensure that projected points matched the actual surface of the meshes. Curve and surface sliding semi-landmarks were then slid to minimize the bending energy of a thin plate spline (TPS) between each specimen and the template at first, and then four times between the result of the previous step and the Procrustes consensus of the complete dataset. Therefore, all landmarks can be treated at the end as geometrically homologous (Gunz, Mitteroecker & Bookstein, 2005). After the sliding step, we performed a Generalized Procrustes Analysis (GPA) to remove the effect of size, location and orientation of the different landmark conformations (Gower 1975; Rohlf & Slice 1990). Projection, relaxation, sliding processes and GPA were conducted using the "Morpho" package (v2.7) in the R environment (v3.5.1—R Core Team, 2014). Details of the process are provided in the documentation of the package (Schlager 2017).

Study of morphological integration

We explored fifteen covariation patterns among all the possible pairs of bones (Gasc 2001; Schmidt & Fischer 2009): within-limbs adjacent bones (humerus-radius, humerus-ulna, radius-ulna, femur-tibia, femur-fibula and tibia-fibula), serially homologous bones (humerus-femur, radius-tibia, radius-fibula, ulna-tibia and ulna-fibula) and functionally analogous bones (humerus-tibia, humerus-fibula) (Figure 1). If the serial homology for the stylopodial bones seems obvious, no clear consensus exists for the serial homology within the zeugopodium elements. Many studies consider the radius and the tibia, and the ulna and the fibula, as serially homologous respectively (Bininda-Emonds et al. 2007; Schmidt & Fischer 2009; Martín-Serra et al. 2015; Hanot et al. 2017; Botton-Divet et al. 2018), unfortunately without strong developmental or genetic evidences. Recent studies tend to indicate that the apparently obvious homology between fore- and hind limb segments might be much more spurious than previously thought (Diogo & Molnar 2014; Sears et al. 2015). In this context, we therefore tested the four possible bone combinations in the zeugopodium. As the appendicular skeleton is known to be highly integrated among quadrupedal mammals (Schmidt & Fischer 2009; Martín-Serra et al. 2015; Hanot et al. 2017; Botton-Divet et al. 2018), we also tested the combinations involving non-homologous or analogous bones (radius-femur and ulna-femur) (Figure 1). Covariation patterns were investigated using Two-Blocks Partial Least Squares (2BPLS) analyses. The 2BPLS method extracts the principal axes of covariation from a covariance matrix computed on

two shape datasets (Rohlf & Corti 2000; Botton-Divet et al. 2018; Hanot et al. 2018), allowing to visualise the specimen repartition relatively to these axes and the shape changes associated.

Each PLS axis is characterized notably by its explained percentage of the overall covariation, its PLS correlation coefficient (rPLS) and its p-value, computed as a singular warp analysis as detailed in Bookstein et al. (2003). The p-value was considered as significant when the observed rPLS was higher than the ones obtained from randomly permuted blocks (1000 permutations). When the p-value was below 0.05, the PLS was considered as significant, i.e. the two considered blocks as significantly integrated. We used the function “pls2b” in the “Morpho” package to compute the 2BPLS (Schlager 2017). To visualise these shape changes along the PLS axes, we used the function “plsCoVar” in the “Morpho” package to compute theoretical shapes at two standard deviations on each side of each axis (see Schlager, 2017). These theoretical conformations were then used to calculate a TPS deformation of the template mesh and therefore visualise the shape changes along the PLS axes. We then used the function “meshDist” in the “Morpho” package to create colour maps indicating the location and the intensity of the covariation between two meshes by mapping the distance between the minimum and maximum theoretical shapes along he first PLS axis (i.e. areas in red are the ones showing the most of shape changes within a bone pair whereas the areas in blue are the ones showing the less of shape change).

This procedure was performed at an interspecific level including all the 50 specimens into a single GPA. We also explored the intraspecific level of covariation by performing the sliding and GPA procedures on subsamples containing each different species. We then obtained five specific datasets on which were performed 2BPLS analyses.

Effect of the allometry

It has been previously demonstrated that centroid size may be a good approximation of the body mass of the specimen (Ercoli & Prevosti 2011; Cassini et al. 2012), notably among modern rhinos (Mallet et al. 2019). To assess the effect of body mass on integration patterns – i.e. the effect of evolutionary allometry – we computed a multivariate regression of the shape against the centroid size using the function “procD.lm” in the “geomorph” package (v3.1.2—Adams & Otárola-Castillo, 2013). Then the residuals were used to compute allometry-free shapes, which were analysed with 2BPLS as described previously. Each species may have its own allometric slope, making it difficult to remove the general allometry effect (Klingenberg 2016). However, considering previous results on rhino long bones indicating close allometric slopes for the different species (Mallet et al. 2019) and the reduced sample size inherent to studying this endangered group, we chose to provide allometry-free shapes considering a single allometric component among all species (evolutionary allometry).

Statistical corrections for multiple comparisons

As explained above, we performed multiple pairwise comparisons when computing the different PLS. Each analysis tested a different pair of bones and contained part of the data present in some other analyses (e.g., landmarks of the humerus are tested for covariation with those of the radius, but also in all other pairs involving the humerus). For each tested pair, the hypothesis was that of a significant covariation between the shapes of the two bones. Given these settings and the exploratory approach of the study, there is no common agreement in the literature regarding whether or not statistical corrections for multiple comparisons should be used in the present case in order to lower the risk of finding false positives (i.e. finding a significant result due to chance) (Cabin & Mitchell 2000; Streiner & Norman 2011). In this context, we chose to present and discuss both uncorrected and corrected analyses for multiple comparisons, especially for the analyses at the intraspecific level where the correction had a higher impact (see Results). We applied a Benjamini-Hochberg correction to our data (Benjamini & Hochberg 1995) as described by Randau & Goswami (2018) in a similar context of covariation tests on 3D geometric morphometric data. The test was run in R using the function "p.adjust" in the "stats" package. This correction was applied to all our tests at the interspecific and intraspecific levels.

Results

Covariation at the interspecific level

All the first PLS axes are highly significant (p-values < 0.01 after correction – see Figures 2 and 3). These first axes gather between 53% (tibia-fibula) and 90% (humerus-femur) of the total covariation. Similarly, the rPLS values are high and vary between 0.72 (tibia-fibula) and 0.94 (humerus-ulna), indicating a strong general integration of the limb bones (Figure 4A). Intra-limb bones covary slightly more strongly in the forelimb than in the hind limb (Figure 4A). Surprisingly, the humerus and the ulna covary slightly more together (rPLS = 0.94) than the radius-ulna pair (rPLS = 0.93). In the hind limb, despite a high degree of covariation between the femur and the tibia (rPLS = 0.89), these two bones are poorly integrated with the fibula. When looking at serially homologous bones, the integration appears stronger between the humerus and the femur (rPLS = 0.93) and the ulna and the tibia (rPLS = 0.92) than between the radius and the tibia (rPLS = 0.88) and the ulna and the fibula (rPLS = 0.82). The radius-fibula covariation is the weakest (rPLS = 0.76) of all serially homologous bones. Regarding the functionally analogous bones, the covariation between the humerus and the hind limb zeugopodial bones is strong and more marked with the tibia (rPLS = 0.92) than with the fibula (rPLS = 0.84). Finally, the non-homologous or functionally analogous bones reveal also a stronger covariation between the ulna and the femur (rPLS = 0.90) than between the radius and the femur (rPLS = 0.84). In summary, all categories of pairwise comparisons (intra-limb, serial homology, functional analogy, non-homologous or analogous bones) showed high but unequal degrees of covariation. The fibula particularly stands out as having relatively weak degrees of covariations with other bones, being the only one not showing at least one very high covariation with another bone.

All plots of the first PLS axes are structured by an opposition between *Ds. sumatrensis* in the negative side and *C. simum* in the positive side (Figures 2 and 3), except for the tibia-fibula pair. *Diceros bicornis*, *R. sondaicus* and *R. unicornis* generally plot between these two extremes. All PLS plots involving the humerus display a clear isolation of these three taxa around null values and poorly dispersed clusters (Figure 2A-E). The clusters along the first PLS axis appear structured by a distinction between Asiatic and African taxa (less marked for the humerus-radius [Figure 2A] and the humerus-ulna [Figure 2E] couples) which can reflect an effect of the phylogeny (if considering African and Asiatic groups as sister taxa). This separation between African and Asiatic taxa follows the distribution of body mass within those groups, the lightest species showing the most negative values and the heaviest ones the most positive ones within both geographic groups. For all the bone pairs not involving the humerus, specimens within each species are more widely distributed in the morphospace and are organized differently along the first PLS axis. The radius-ulna first axis clearly

expresses a sorting of the species from the lightest (*Ds. sumatrensis*) on the negative side to the heaviest (*C. simum*) on the positive side (Figure 2F) independently of the phylogenetic affinities between species. Although less clear, this structure also occurs for the radius-femur, radius-fibula, ulna-femur, ulna-fibula and femur-tibia pairs (Figure 2G and Figure 3B, C, E, F). *Dicerorhinus sumatrensis* is strongly isolated on the negative side on all pairs involving the femur (Figure 2C, G and Figure 3C, F, G). A third pattern isolating *Ds. sumatrensis* and *Dc. bicornis* on the negative part from the three other species on the positive part can be observed for the radius-tibia and ulna-tibia pairs (Figure 3A, D). The only first PLS axis showing a clearly different pattern is that of the tibia-fibula pair, where *R. sondaicus* is the most extreme species on the positive part and *C. simum* and *R. unicornis* clusters overlap (Figure 3H).

The second PLS axes are significant in most of the cases, except for the humerus-radius and humerus-femur pairs (p-values > 0.05 – see Supporting Information Figures S3). These second axes explain between 4% (humerus-femur) and 31% (ulna-tibia) of the global covariation. Most of the PLS plots indicate a separation between the genus *Rhinoceros* and the three other rhino species, with an important overlapping of the clusters in many cases (see Supporting Information Figure S3). This distinction is however absent for most of the plots involving the fibula, where the genus *Rhinoceros* may overlap the *D.* or *D.* clusters. No clear intraspecific pattern linked to age or sex has been found along these second PLS axes.

Colour maps computed using the theoretical shapes (available in the Supplementary Figure S4) indicate that covariation associated to the first PLS axes are very similar for each bone regardless of the considered pair. Eight pairs representing the four types of relation existing between bones are presented in Figure 5 and 6. All other pairs are available in Supplementary Figure S5. The shape changes are mainly related to an increase of the bone robustness from negative to positive values of the axes, associated to a development of most of the muscular insertions (tubercles and trochanters) and of articular surfaces. For the humerus, most of the shape covariation with the other bones is located on muscular insertion areas, such as the lesser tubercle, the deltoid tuberosity, the lesser tubercle convexity and the epicondylar crest, where insert respectively the *m. supraspinatus*, the *m. deltoideus*, the *m. subscapularis* and the *m. extensor carpi radialis* (Figure 5A and 5D). The intensity of the covariation of the deltoid tuberosity is higher with the radius than with all other bones. For the radius, the strongest shape covariation with the other bones is located on the lateral insertion relief where inserts the *m. extensor digitorum communis*, on the medial part of the distal epiphysis and, to a lesser extent, on the radial tuberosity where inserts the *m. biceps brachii* (Figure 5B and 6A). On the medial part of the distal epiphysis, the shape covariation is less intense in the humerus-radius and radius-fibula couples than in the other bone pairs. For the ulna, the shape covariation with the

other bones is mainly located on the medial and lateral tuberosities of the olecranon (where insert respectively the medial and lateral heads of the *m. triceps brachii*) and along the lateral and palmar edges of the shaft, where insert most of the digit extensors (Figure 5C, 6A and 6D). The shape covariation is slightly more pronounced on the olecranon tuberosity in the radius-ulna pair than in the other pairs. The femur is the bone showing the most similar patterns of shape covariation regardless of the bone pair. The strongest shape covariation with all other bones is located on the third tubercle and corresponds to the insertion of the *m. gluteus superficialis*. Other strong shape covariations between the femur and the other bones are located on the greater trochanter convexity where inserts the *m. gluteus accessorius*, and from the *fovea capitis* to the lesser tubercle where insert both the *mm. psoas major* and *iliacus* as well as the joint capsule of the hip (Figure 5A, 6B and 6D). Unlike the femur, the patterns of shape covariation for the tibia are highly variable depending of the considered bone pair. For the radius-tibia and the ulna-tibia pairs, the strongest shape covariation is mainly located on the tibial tuberosity (where insert notably the medial, intermediate and lateral patellar ligaments, the patellar fascia and the *fascia lata*), the tibial crest, the area located distally to the medial condyle of the tibia where inserts the *m. popliteus*, and on the cranial and caudal sides of the distal part of the shaft (Figure 5B). The shape covariation is located in the same areas but with less intensity for the femur-tibia and tibia-fibula pairs (Figure 6B and 6C). The intensity of the shape covariation is minimal for the humerus-tibia pair, except for the insertion of the *m. popliteus* (Figure 5D). Finally, for the fibula, the shape covariation with the other bones is mainly located on the cranial part of the head of the fibula, on the distal part of the cranial crest and on the caudal crest along the shaft, where insert notably the digit extensors (Figure 5C and 6C).

Allometry-free covariation

All the first PLS axes computed on allometry-free shapes are highly significant (p-values after correction < 0.01 – see Figures 7 and 8). The first PLS axes explain between 44% (ulna-fibula) and 87% (humerus-femur) of the total covariation. The rPLS values remain high and range between 0.70 (humerus-radius) and 0.91 (humerus-femur). The rPLS values are unequally impacted by the correction for allometry depending on the considered bone pair. A drop of 12 – 16% of the rPLS values can be observed between raw and allometry-free shapes for some couples: two intra-limbs pairs (humerus-radius, humerus-ulna) and two non-homologous or functionally analogous bones (radius-femur and ulna-femur) (Figure 4B). The drop of the rPLS values is less marked for other pairs and almost inexistent in the humerus-femur, humerus-fibula and ulna-fibula couples. Moreover, the

rPLS value is strictly the same for the radius-fibula pair. We also noticed a slight rise of the rPLS value for the femur-fibula and tibia-fibula pairs by 6% and 1% respectively.

However, the distribution of the different species and specimens along the first PLS axes is different from the previous analyses (Figures 2 and 3) when computed on allometry-free shapes (Figures 7 and 8). All plots involving the humerus are structured in the same way with a strong separation between the three Asiatic species on the negative side and the two African species on the positive side (Figure 7A-E). A relatively similar structure is observed for the ulna-femur plot (Figure 8C) but the patterning of the distribution for all other bone pairs distributions is far less clear. Plots for the radius-ulna and the radius-tibia pairs display a similar pattern with *Dc. bicornis* and *Ds. sumatrensis* grouped together on the negative side, and the three other species on the positive side (Figure 7F and Figure 8A) despite some overlaps. Other plots display various patterns not distinguishing the species based on either size, geography or phylogenetic relationships. We can notably see an opposition between *R. unicornis* and *C. simum* at the positive and negative parts of the first axis respectively with *Ds. sumatrensis* and *Dc. bicornis* overlapping around null values for the ulna-fibula pair (Figure 8E), or a slight distinction between the *Rhinoceros* genus and the other species for the ulna-tibia pair, whereas *Dc. bicornis* and *R. sondaicus* are strictly opposed along the first PLS axis (Figure 8D). A separation between *R. sondaicus* and the other species is also clearly visible for the tibia-fibula pair (Figure 8H). As for the raw data, the allometry-free shape changes along the first PLS axes mainly concern the robustness of the bones and shape covariation is very similar for all the bones regardless of the considered pair. All allometry-free theoretical shapes are available in the Supplementary Figure S6.

Intraspecific covariation

Without Benjamini-Hochberg correction

At the intraspecific level, rPLS values are relatively high but few first PLS axes are statistically significant, even before correction (Table 2). Analyses reveal that the first PLS axis is significant for five bone pairs within *C. simum* (humerus-radius, humerus-ulna, humerus-femur, radius-femur and ulna-femur) and *R. sondaicus* (humerus-radius, radius-tibia, radius-fibula, humerus-tibia and ulna-femur), three for *R. unicornis* (humerus-ulna, tibia-fibula and ulna-tibia), two for *Ds. sumatrensis* (humerus-femur and humerus-tibia) and only one for *Dc. bicornis* (ulna-tibia). The rPLS values are extremely high (from 0.89 to 0.99) for *R. sondaicus* relatively to the other species (0.72 - 0.94 for *C. simum*, 0.66 - 0.96 for *Ds. sumatrensis*, 0.76 - 0.96 for *Dc. bicornis* and 0.79 - 0.97 for *R. unicornis*). Although the covariation of some pairs may be common to some taxa (e. g. humerus-radius and ulna-femur for *C. simum* and *R. sondaicus*, humerus-tibia for *Ds. sumatrensis* and *R. sondaicus*), each

species displays an overall different pattern of covariation. The observed lacks of significance may be due to the small number of specimens per species. However, *C. simum* and *R. sondaicus* show the highest percentage of significant results and are respectively represented by 15 and 7 specimens, these two subsamples being not particularly more diverse than the other species (adults and subadults, males and females, wild and captive specimens – see Supplementary Figure S7). This indicates that the observed tendency is not only related to the sample size but may also carry some biological signal. Moreover, some bone pairs show a p-value between 0.05 and 0.1 associated with a high rPLS value. This is notably the case for the tibia-fibula pair in the two *Rhinoceros* species (Table 2). This tends to indicate that the shape covariation between the fibula and the tibia may be higher for this clade than for other rhino species. In addition, the rPLS values of other pairs involving the fibula are often higher in both species of *Rhinoceros* than in other species in our sample, although their covariation is rarely significant.

For all these pairs, shape covariation involves anatomical areas which are similar within each species but often different between species (see Supplementary Figure S8). However, some anatomical areas appear to show high shape covariation both at the interspecific and intraspecific levels. This is notably the case of the greater tubercle convexity and the deltoid tuberosity of the humerus and the olecranon tuberosity of the ulna. These areas correspond to the insertion of powerful muscles for flexion and extension of the forearm (respectively the *m. infraspinatus*, the *m. deltoideus* and the *m. triceps brachii*).

After Benjamini-Hochberg correction

After the Benjamini-Hochberg correction of the p-values, rPLS values remain statistically significant for only four bone pairs, all belonging to *C. simum*, which is the species with the highest number of specimens (Table 2). In this species, the covariation is extremely strong for the humerus-radius (rPLS = 0.92), the humerus-femur (rPLS = 0.93) and the ulna-femur (rPLS = 0.94) pairs, and slightly weaker for the radius-femur pair (rPLS = 0.89). When looking at the first PLS axes for these four bone pairs, it appears clearly that the subadults are separated from the adults, sometimes without overlap, as for the ulna-femur pair (Figure 9). Contrary to the age class, the size of the individuals (expressed by the sum of the centroid sizes of the two bones in each case) does not seem to follow a precise pattern along the first PLS axes for these four bone pairs (Figure 9). A slight distinction between males and females observed along the first PLS axes may partly account for the sexual dimorphism that exists in this species (Groves 1972; Guérin 1980). However, our data are not sufficient to state on a potential difference of integration level due to sexual dimorphism in *C. simum*.

Although not statistically significant before and after correction, similar distinctions between adults and subadults have been observed on the first PLS axes for *Dc. bicornis* for some bone pairs (mainly humerus-radius, humerus-ulna, humerus-femur, humerus-tibia and radius-femur). Details on age class are too often missing for the three Asiatic species to state on this aspect. Shape variation associated to the first PLS axes in the significant covariations after correction in *C. simum* show a different tendency than at the interspecific level. The increase in robustness mainly concerns the shaft of the bone, both epiphyses tending to be already very large in subadults. This is particularly the case for the humerus and the femur (Figure 10). Colour maps confirm that the shape covariation along the first PLS axes for *C. simum* concerns different areas than at the interspecific level, with a different intensity depending on the bone pairs (Figure 10). We can notably observe that the cranial side of the femur covaries strongly with the humerus and the radius, but visibly less with the ulna (Figure 10B, C and D). However, some anatomical areas are similarly affected by shape covariation both at the intra- and interspecific levels. This is notably the case for the lesser tubercle tuberosity on the humerus (insertion of the *m. subscapularis*) (Figure 10A and B) and the greater trochanter convexity on the femur (insertion of the *m. gluteus accessorius*) (Figure 10B and C).

Discussion

Patterns of evolutionary integration

Our results indicate that the limb long bones of modern rhino species are strongly integrated at the interspecific level, confirming our first *a priori* hypothesis. This tendency has been previously observed on limb bones among other terrestrial mammal groups, notably in equids (Hanot et al. 2017, 2018, 2019), but also in more phylogenetically distant and older clades such as carnivorans (Fabre et al. 2014; Martín-Serra et al. 2015; Botton-Divet et al. 2018) and marsupials (Martín-Serra & Benson 2019). The high shape covariation between functionally analogous bones (humerus-tibia) as well as between non-analogous bones (ulna-femur) tends to indicate that this strong general integration may be related to a highly coordinated locomotion, as observed in equids at the interspecific level (Hanot et al. 2017), which is coherent with the rhino ability to gallop (Alexander & Pond 1992) and to reach high running speed (Blanco et al. 2003).

However, contrary to our second hypothesis, this integration is unequally distributed among the tested pairs of bones. The within-limb integration is slightly stronger in the forelimb than in the hind limb, whereas in other taxa, the morphological integration is generally higher in the hind limb (Martín-Serra et al. 2015; Hanot et al. 2017; Botton-Divet et al. 2018). The covariation is maximal for the humerus-ulna and the radius-ulna couples. Although the femur and the tibia display a strong covariation with one another, the fibula appears as the bone showing the lowest integration level. This is consistent with previous observations on morphological variation of rhino long bones, highlighting that the shape of the fibula is highly variable at the intraspecific level (Mallet et al. 2019). Therefore, the apparent lower integration of the hind limb may be mainly due to the independent shape variation of the fibula. The fibula appears nevertheless to be more strongly integrated with the humerus (functionally analogous) and the ulna (serially homologous) than with other hind limb bones. This confirms that the shape of the fibula remains covariant with other bones beyond stochastic variation, potentially driving the slightly lower integration of the hind limb than of the forelimb.

Body mass and evolutionary integration

Within limbs

Among modern rhinos, most of the shape covariation is mainly driven by an increase in general robustness and in the size of the articular surfaces and muscular insertion areas. This is coherent with previous observations on other quadrupedal mammals (Martín-Serra et al. 2015; Botton-Divet et al.

2018; Hanot et al. 2018). The correction for allometry affects both the rhino species distribution along the PLS axes and the rPLS values in a stronger way than for equids (Hanot et al. 2018), carnivorans (Martín-Serra et al. 2015) or musteloids (Botton-Divet et al. 2018) at the interspecific level, confirming our third hypothesis specifying that body mass has a stronger influence on the degree of integration among heavy quadrupedal than in lighter mammal species. Allometry is also clearly more pronounced on the forelimb than on the hind limb, as shown by the drastic reduction of the integration intensity when using the allometry-free shapes. This tends to indicate that beyond the strong general integration of the rhino limb bones, the overall higher integration within the forelimb might be caused by a stronger allometry in these bones – and thus more strongly affected by body mass (Ercoli & Prevosti 2011; Cassini et al. 2012; Mallet et al. 2019) – than the hind limb. Heavy quadrupeds bear a larger part of the body weight on their forelimbs than on their hind limbs (Hildebrand 1974) and rhinos follow this body plan (Regnault et al. 2013) due to their heavy head and horns and their massive trunk muscles and bones. Previous observations (Schmidt & Fischer 2009; Hanot et al. 2018) led to the conclusion that body mass can contribute to covariation between bones, which our data seem to confirm for rhinos. The higher integration of the forelimb may thus be interpreted as a specialization linked to weight bearing (Martín-Serra et al. 2015; Randau & Goswami 2018).

Furthermore, the covariation of the different elements composing the forelimb is probably related to a complementary effect of phylogenetic relationships, developmental constraints and body mass. The shape covariation between the humerus and the zeugopodium elements in the forelimb is clearly driven by a distinction between Asiatic and African species, associated with a sorting linked to the mean body mass within these two groups. The covariation is particularly strong between the humerus and the ulna, and although it seems to be largely patterned by phylogenetic history, this is congruent with previous studies indicating a high integration level between the bones involved in flexion/extension movements and body stability (Fabre et al. 2014). Conversely, the interspecific covariation of the radius-ulna pair seems intimately linked to the mean body mass of rhino species, with no distinct link to the phylogenetic pattern. This indicates a likely major impact of mass on the zeugopodium integration coupled with a common developmental origin (Young & Hallgrímsson 2005; Sears et al. 2007). These results are also in good agreement with the more important impact of body mass observed on the shape of the radius and ulna than on that of the humerus (Mallet et al. 2019) and the role of the zeugopodium in the support of the body weight due to the alignment of this segment with pressure forces (Bertram & Biewener 1992).

Albeit less obvious, an effect of body mass on the hind limb interspecific integration could also exist, especially between the femur and the tibia when looking at the species distribution along the first PLS axis (raw shapes) and the rPLS values for allometry-free shapes. In a similar way than for the forelimb, these two bones are involved in leg flexion/extension, particularly for propulsion (Hildebrand 1974; Lawler 2008; Biewener & Patek 2018). Conversely, the degree of integration increases between the femur and the fibula (and to a lesser extent between the tibia and the fibula) when the allometric effect is removed, which is a unique phenomenon among all tested limb bone pairs. One interpretation can be that the allometry effect consists in antagonistic changes between the femur and the fibula, and that the fibula shape covariation at the interspecific level is poorly related to body mass. This is coherent with all low rPLS drops for allometry-free shapes in all other pairs involving the fibula. This difference can also be influenced by a different covariation between the femur and the fibula depending on the rhino species (see below). The independence of the shape variation of the fibula relatively to the tibia also indicates that, contrary to the forelimb zeugopodium, neither common developmental origin nor functional requirements seem to highly constrain the covariation between the two hind limb zeugopodium bones.

Following the hypotheses of Hallgrímsson et al. (2002) and Young & Hallgrímsson (2005) stating that a functionally specialized part covaries less with surrounding elements, the fibula could be interpreted as a highly specialized bone in some rhino species. However, as previously observed for the ulna of musteloids (Botton-Divet et al. 2018), the lower integration of the fibula may be linked to a decrease of the functional constraints exerted on this bone. The fibula supports the insertion of digit flexors and extensors (Barone 2010) and is involved in the ankle stability and weight bearing among rhinos. However the fibula shape has been proven to be poorly correlated with body mass (Mallet et al. 2019). Therefore, it is likely that the fibula shape varies more independently and is less functionally constrained by body mass than other limb bones in some rhino species (see below). This may be interpreted as a case of parcellation (Young & Hallgrímsson 2005) due to a functional dissociation between the bones of a single limb.

All the pairs involving the humerus seem thus more strongly impacted by phylogeny than by functional constraints and, to a lesser extent, by body mass. Most of the other bone pairs rather suggest a dominant effect of body mass, especially the ones involving the radius and the ulna. Although less clear, similar results are obtained for the hind limb bones.

Between limbs

At the interspecific level, serially homologous bones are strongly integrated but their covariation is differently associated with body mass, i.e. more for the zeugopodium elements than for the stylopodium ones. Together with the slightly lower integration values of the zeugopodium elements relatively to the stylopodium, these observations are also coherent with previous studies indicating a decrease of the integration from proximal to distal parts of the limbs linked to a higher degree of specialization of distal elements (Young & Hallgrímsson 2005). In addition, our results are not congruent with the strict serial homology classically considered for the zeugopodium (radius-tibia and ulna-fibula) by showing a stronger covariation between the ulna and the tibia than between the radius and the tibia. Similar results were observed on carnivorans and interpreted as a potential functional convergence between these bones (Martín-Serra et al. 2015). These results could also revive doubts on the *a priori* hypothesis of homology between zeugopodium bones, which has long been debated (Owen 1848; Wyman 1867; Lessertisseur & Saban 1967) and, to our knowledge, still remains unresolved although largely taken for granted (i.e. Bininda-Emonds et al. 2007; Bennett & Goswami 2011; Martín-Serra et al. 2015; Botton-Divet et al. 2018). Only a comprehensive study of the genetic processes leading to the development of forelimb and hind limb zeugopodium could clarify this aspect (Klingenberg 2014).

The strong integration between the humerus and the tibia (and the fibula to a lesser extent) tends to confirm the functional analogy between the forelimb stylopodium and the hind limb zeugopodium (Gasc 2001; Schmidt & Fischer 2009). However, the shape covariation is weaker in the humerus-tibia pair than in other bone pairs involving the tibia (e.g. radius-tibia and ulna-tibia), which tends to indicate that, in the present case, the functional requirements linked to locomotion and body support during resting time may less affect the shape covariation than the developmental constraints, contrary to what has been observed in lighter taxa (Fabre et al. 2014; Hanot et al. 2017; Botton-Divet et al. 2018). Moreover, the high covariation between the ulna and the femur also tackles the classic functional approach, highlighting a strong integration between non-homologous or analogous bones, an observation also recently revealed among marsupials (Martín-Serra & Benson 2019). Recent work using a network approach on a phylogenetic matrix of characters among modern and fossil rhinos showed that unexpected covariations can exist between cranial, dental and postcranial phenotypic traits in the group (Lord et al. 2019). In particular, the authors observed a frequent co-occurrence of discrete traits between the radius-ulna and the femur among all rhinos, which seems coherent with our results indicating a strong covariation between the forelimb zeugopodium and the hind limb stylopodium. Since the postcranial body plan appears to be implemented early during the Rhinocerotoidea evolutionary history (Lord et al. 2019) and may be less variable than in phylogenetically-close taxa like equids (McHorse et al.

2019), this may imply strong inherited developmental constraints within this group canalizing the shape covariation (Hallgrímsson et al. 2002) even between non-homologous bones. Furthermore, the high integration of non-homologous or analogous bones appears as strongly congruent with the variation in body mass, lending further support to the link between heavy weight and high general integration level (Schmidt & Fischer 2009; Hanot et al. 2017).

Covariation at the intraspecific level: developmental integration

Our exploration of integration patterns at the intraspecific level is limited by the low sample size for all species and the non-significance (at $p>0.05$) of most of the PLS axes obtained for the different pairs of bones, particularly after the Benjamini-Hochberg correction. Beyond this strict non-significance (which is currently criticized in favour of a more continuous approach of the p-value – see Ho et al. 2019; Wasserstein et al. 2019), no clear similar pattern of integration seems to emerge between light and heavy rhino species, or between African and Asiatic species. Some species share the same significant or almost significant bone pairs. The covariation between the tibia and the fibula among *Rhinoceros* notably seems relatively strong as compared to in other species, confirming previous results on individual shape variation (Mallet et al. 2019). This aspect may indicate that the hind limb zeugopodium – and particularly the fibula – is less variable among the two species of this genus, with a lesser parcellation among this group.

The integration patterns found in *C. simum,* the species with the most specimens, reveal both similarities and divergences with the patterns observed at the interspecific level (i.e. evolutionary integration, see Cheverud 1996; Klingenberg 2014). All the significant PLS axes in this species concern forelimb bones and indicate a very strong integration between the humerus, the radius and the ulna, as well as a high shape covariation between the humerus and the femur (serial homology). The strong integration of the forelimb may be partly related to the heavier and longer head of *C. simum* compared to other species (Guérin 1980) and highlights different patterns of distribution of body weight among modern rhinos (Antoine, pers. obs. 2020). The shape covariation among *C. simum* specimens reveals a strong effect of age with a clear separation between adults and subadults in all cases. Even if this effect is not visible at the interspecific level, the separation between the two age classes is the main driver of the integration within this species, whereas body mass (approximately expressed through the value of the centroid size) and sex do not seem to play a visible role on the covariation patterns. This tendency is associated with a shape covariation on anatomical areas often different to the ones showing a strong covariation at the interspecific level. Only the greater tubercle convexity and the deltoid tuberosity on the humerus, the

572 olecranon tuberosity on the ulna and the greater trochanter convexity on the femur show a high degree
573 of shape covariance both at both interspecific and intraspecific levels.

574 Within *C. simum*, developmental integration is more related to proportions between the different bone
575 parts (e.g. shaft and epiphyses) than to the development of powerful muscular insertions ensuring the
576 stability and the locomotion of the body. In the end, the global integration of the rhino limb long bones
577 results in the superposition and association of the different levels of integration (here, developmental
578 and evolutionary). These integration levels are conjointly influenced by shared phylogenetic history,
579 similar developmental origin and constraints due to both locomotion and body mass support (Cheverud
580 1996; Hallgrímsson et al. 2009; Klingenberg 2014). Investigated here among *C. simum*, the static and
581 developmental integration levels remain to be explored with a larger sample for the other rhino species
582 – which remains challenging for these endangered species. Finally, the addition of some of the numerous
583 fossil taxa belonging to the superfamily Rhinocerotoidea and displaying convergent increases of body
584 mass will help testing the influence of body mass on integration patterns suggested in the present study
585 (Klingenberg 2014).

Conclusion

Our exploration of the integration patterns of the limb long bones among modern rhinos reveals that the appendicular skeleton of these species is strongly integrated, as in other terrestrial quadrupedal mammals. At the interspecific level, the forelimb appears as more covariant than the hind limb, with a more apparent relation to body mass, which appears stronger than for more lightly built terrestrial mammals. This can be interpreted as a higher degree of specialization of the forelimb in body weight support. Proximal elements appear primarily affected by common developmental constraints whereas the distal parts of the limbs seem rather shaped by functional requirements, which would confirm hypotheses addressed on different mammal groups. The appendicular skeleton of rhinos appears to be a compromise between the functional requirements of a highly coordinated locomotion, the necessity to sustain a high body mass and important inherited developmental processes constraining shape covariation – located mostly on insertion areas for powerful flexor and extensor muscles. In addition, the exploration of the shape covariation at the intraspecific level reveals a prominent effect of the age class in shaping the covariation patterns among *C. simum*. These results are a first step to explore further the functional construction of the appendicular skeleton of modern rhinos and to extend this approach to other heavy modern taxa (such as elephants or hippos). Moreover, the numerous fossil taxa composing the superfamily Rhinocerotoidea and showing a broad range of body mass would be a valuable group to extend these results and highlight convergent patterns of shape covariation directly linked to a heavy weight.

Acknowledgments

The authors would like to warmly thank all the curators of the visited institutions for granting us access to the studied specimens: E. Hoeger and S. Ketelsen (American Museum of Natural History, New York, USA), C. West, R. Jennings, M. Cobb (Powell Cotton Museum, Birchington-on-Sea, UK), D. Berthet (Centre de Conservation et d'Étude des Collections, Musée des Confluences, Lyon, France), J. Lesur, A. Verguin (Muséum National d'Histoire Naturelle, Paris, France), R. Portela-Miguez (Natural History Museum, London, UK), F. Zachos, A. Bibl (Naturhistorisches Museum Wien, Vienna, Austria), O. Pauwels, S. Bruaux (Royal Belgian Institute of Natural Sciences, Brussels, Belgium), E. Gilissen (Royal Museum for Central Africa, Tervuren, Belgium) and A. H. van Heteren (Zoologische Staatssammlung München, Munich, Germany). C.M. acknowledges C. Étienne, R. Lefebvre (MNHN, Paris, France) and P. Hanot (Max Planck Institute for the Science of Human History, Jena, Germany) for constructive discussions and advices on R programming, data analyses and interpretations. All authors would like to thank P.-O. Antoine (University of Montpellier, France) and another anonymous reviewer for their comments that helped to improve the quality of the manuscript, as well as A. Graham (King's College London, UK) for editorial work. This work was funded by the European Research Council and is part of the GRAVIBONE project (ERC-2016-STG-715300).

Author contributions

C.M. designed the study with significant inputs from A.H., R.C. and G.B. C.M. did the data acquisition with inputs from A.H. C.M. performed the analyses with the help of R.C and all authors interpreted the results. C.M. drafted the manuscript. All authors reviewed and contributed to the final version of the manuscript, read it and approved it.

References

Adams DC, Otárola-Castillo E (2013) geomorph: an r package for the collection and analysis of geometric morphometric shape data. *Methods in Ecology and Evolution* **4**, 393–399. doi:10.1111/2041-210X.12035.

Adams DC, Rohlf FJ, Slice DE (2004) Geometric morphometrics: Ten years of progress following the 'revolution.' *Italian Journal of Zoology* **71**, 5–16. doi:10.1080/11250000409356545.

Agisoft (2018) *PhotoScan Professional Edition*, Agisoft.

Alexander RMcN, Pond CM (1992) Locomotion and bone strength of the white rhinoceros, Ceratotherium simum. *Journal of Zoology* **227**, 63–69. doi:10.1111/j.1469-7998.1992.tb04344.x.

Antoine P-O (2002) Phylogénie et évolution des Elasmotheriina (Mammalia, Rhinocerotidae). *Mémoires du Muséum National d'Histoire Naturelle (1993)* **188**, 5–350.

Artec 3D (2018) *Artec Studio Professional*, Artec 3D.

Baker J, Meade A, Pagel M, et al. (2015) Adaptive evolution toward larger size in mammals. *PNAS* **112**, 5093–5098. doi:10.1073/pnas.1419823112.

Bardua C, Felice RN, Watanabe A, et al. (2019) A Practical Guide to Sliding and Surface Semilandmarks in Morphometric Analyses. *Integr Org Biol* **1**. doi:10.1093/iob/obz016.

Barone R (2010) *Anatomie comparée des mammifères domestiques. Tome 1 : Ostéologie* 5ème édition., Paris: Vigot Frères.

Bell E, Andres B, Goswami A (2011) Integration and dissociation of limb elements in flying vertebrates: a comparison of pterosaurs, birds and bats. *Journal of Evolutionary Biology* **24**, 2586–2599. doi:10.1111/j.1420-9101.2011.02381.x.

Benjamini Y, Hochberg Y (1995) Controlling the False Discovery Rate: A Practical and Powerful Approach to Multiple Testing. *Journal of the Royal Statistical Society: Series B (Methodological)* **57**, 289–300. doi:10.1111/j.2517-6161.1995.tb02031.x.

Bennett CV, Goswami A (2011) Does developmental strategy drive limb integration in marsupials and monotremes? *Mammalian Biology* **76**, 79–83. doi:10.1016/j.mambio.2010.01.004.

Bertram JEA, Biewener AA (1992) Allometry and curvature in the long bones of quadrupedal mammals. *Journal of Zoology* **226**, 455–467. doi:10.1111/j.1469-7998.1992.tb07492.x.

Biewener AA (1983) Allometry of quadrupedal locomotion: the scaling of duty factor, bone curvature and limb orientation to body size. *Journal of Experimental Biology* **105**, 147–171.

Biewener AA (1989a) Mammalian Terrestrial Locomotion and Size. *BioScience* **39**, 776–783. doi:10.2307/1311183.

Biewener AA (1989b) Scaling body support in mammals: limb posture and muscle mechanics. *Science* **245**, 45–48. doi:10.1126/science.2740914.

Biewener AA, Patek SN (2018) *Animal locomotion* Second edition., New York: Oxford University Press.

Bininda-Emonds OR, Jeffery JE, Sánchez-Villagra MR, et al. (2007) Forelimb-hindlimb developmental timing changes across tetrapod phylogeny. *BMC Evolutionary Biology* **7**, 1–7. doi:10.1186/1471-2148-7-182.

Blanco RE, Gambini R, Fariña RA (2003) Mechanical model for theoretical determination of maximum running speed in mammals. *Journal of Theoretical Biology* **222**, 117–125. doi:10.1016/S0022-5193(03)00019-5.

Bokma F, Godinot M, Maridet O, et al. (2016) Testing for Depéret's Rule (Body Size Increase) in Mammals using Combined Extinct and Extant Data. *Syst Biol* **65**, 98–108. doi:10.1093/sysbio/syv075.

Bookstein FL (2015) Integration, Disintegration, and Self-Similarity: Characterizing the Scales of Shape Variation in Landmark Data. *Evol Biol* **42**, 395–426. doi:10.1007/s11692-015-9317-8.

Bookstein FL, Gunz P, Mitterœcker P, et al. (2003) Cranial integration in Homo: singular warps analysis of the midsagittal plane in ontogeny and evolution. *Journal of Human Evolution* **44**, 167–187. doi:10.1016/S0047-2484(02)00201-4.

Botton-Divet L, Cornette R, Fabre A-C, et al. (2016) Morphological Analysis of Long Bones in Semi-aquatic Mustelids and their Terrestrial Relatives. *Integr Comp Biol* **56**, 1298–1309. doi:10.1093/icb/icw124.

Botton-Divet L, Houssaye A, Herrel A, et al. (2018) Swimmers, Diggers, Climbers and More, a Study of Integration Across the Mustelids' Locomotor Apparatus (Carnivora: Mustelidae). *Evol Biol* **45**, 182–195. doi:10.1007/s11692-017-9442-7.

Cabin RJ, Mitchell RJ (2000) To Bonferroni or Not to Bonferroni: When and How Are the Questions. *Bulletin of the Ecological Society of America* **81**, 246–248.

Cappellini E, Welker F, Pandolfi L, et al. (2019) Early Pleistocene enamel proteome from Dmanisi resolves Stephanorhinus phylogeny. *Nature*, 1–5. doi:10.1038/s41586-019-1555-y.

Cassini GH, Vizcaíno SF, Bargo MS (2012) Body mass estimation in Early Miocene native South American ungulates: a predictive equation based on 3D landmarks. *J Zool* **287**, 53–64. doi:10.1111/j.1469-7998.2011.00886.x.

Cheverud JM (1982) Phenotypic, Genetic, and Environmental Morphological Integration in the Cranium. *Evolution* **36**, 499–516. doi:10.1111/j.1558-5646.1982.tb05070.x.

Cheverud JM (1996) Developmental Integration and the Evolution of Pleiotropy. *Integr Comp Biol* **36**, 44–50. doi:10.1093/icb/36.1.44.

Cignoni P, Callieri M, Corsini M, et al. (2008) *MeshLab: an Open-Source Mesh Processing Tool*, The Eurographics Association. doi:http://dx.doi.org/10.2312/LocalChapterEvents/ItalChap/ItalianChapConf2008/129-136.

Cubo J (2004) Pattern and process in constructional morphology. *Evolution & Development* **6**, 131–133. doi:10.1111/j.1525-142X.2004.04018.x.

Depéret C (1907) *Les transformations du monde animal*, Paris: Flammarion.

Dinerstein E (2011) Family Rhinocerotidae (Rhinoceroses). In *Handbook of the Mammals of the World*. Barcelona: Don E. Wilson & Russel A. Mittermeier, 144–181.

Diogo R, Molnar J (2014) Comparative anatomy, evolution, and homologies of tetrapod hindlimb muscles, comparison with forelimb muscles, and deconstruction of the forelimb-hindlimb serial homology hypothesis. *Anat Rec (Hoboken)* **297**, 1047–1075. doi:10.1002/ar.22919.

Eisenmann V, Guérin C (1984) Morphologie fonctionnelle et environnement chez les périssodactyles. *Geobios* **17**, 69–74. doi:10.1016/S0016-6995(84)80158-8.

Ercoli MD, Prevosti FJ (2011) Estimación de Masa de las Especies de Sparassodonta (Mammalia, Metatheria) de Edad Santacrucense (Mioceno Temprano) a Partir del Tamaño del Centroide de los Elementos Apendiculares: Inferencias Paleoecológicas. *Ameghiniana* **48**, 462–479. doi:10.5710/AMGH.v48i4(347).

Fabre A-C, Cornette R, Peigné S, et al. (2013) Influence of body mass on the shape of forelimb in musteloid carnivorans. *Biol J Linn Soc* **110**, 91–103. doi:10.1111/bij.12103.

Fabre A-C, Goswami A, Peigné S, et al. (2014) Morphological integration in the forelimb of musteloid carnivorans. *Journal of Anatomy* **225**, 19–30. doi:10.1111/joa.12194.

Fau M, Cornette R, Houssaye A (2016) Photogrammetry for 3D digitizing bones of mounted skeletons: Potential and limits. *Comptes Rendus Palevol* **15**, 968–977. doi:10.1016/j.crpv.2016.08.003.

Federative Committee on Anatomical Terminology (1998) *Terminologia Anatomica*, Georg Thieme Verlag.

Gasc J-P (2001) Comparative aspects of gait, scaling and mechanics in mammals. *Comparative Biochemistry and Physiology Part A: Molecular & Integrative Physiology* **131**, 121–133. doi:10.1016/S1095-6433(01)00457-3.

Gaudry M (2017) *Molecular phylogenetics of the rhinoceros clade and evolution of UCP1 transcriptional regulatory elements across the mammalian phylogeny*. Master of Science. Winnipeg: University of Manitoba. Available: https://mspace.lib.umanitoba.ca/xmlui/handle/1993/32525. Accessed 15 Oct 2018.

Goswami A, Polly PD (2010) Methods for Studying Morphological Integration and Modularity. *The Paleontological Society Papers* **16**, 213–243. doi:10.1017/S1089332600001881.

Goswami A, Smaers JB, Soligo C, et al. (2014) The macroevolutionary consequences of phenotypic integration: from development to deep time. *Philosophical Transactions of the Royal Society B: Biological Sciences* **369**, 20130254. doi:10.1098/rstb.2013.0254.

Gould SJ (2002) *The Structure of Evolutionary Theory*, Cambridge, Massachusetts; London, England: Harvard University Press. Available: www.jstor.org/stable/j.ctvjsf433. Accessed 22 Nov 2019.

Gower JC (1975) Generalized procrustes analysis. *Psychometrika* **40**, 33–51. doi:10.1007/BF02291478.

Groves CP (1972) Ceratotherium simum. *Mammalian Species*, 1–6. doi:10.2307/3503966.

Guérin C (1980) *Les Rhinocéros (Mammalia, Perissodactyla) du Miocène terminal au Pléistocène supérieur en Europe occidentale. Comparaison avec les espèces actuelles.* Documents du Laboratoire de Géologie de l'Université de Lyon.

Gunz P, Mitteroecker P (2013) Semilandmarks: a method for quantifying curves and surfaces. *Hystrix, the Italian Journal of Mammalogy* **24**, 103–109.

Hallgrímsson B, Jamniczky H, Young NM, et al. (2009) Deciphering the Palimpsest: Studying the Relationship Between Morphological Integration and Phenotypic Covariation. *Evol Biol* **36**, 355–376. doi:10.1007/s11692-009-9076-5.

Hallgrímsson B, Willmore K, Hall BK (2002) Canalization, developmental stability, and morphological integration in primate limbs. *American Journal of Physical Anthropology* **119**, 131–158. doi:10.1002/ajpa.10182.

Hanot P, Herrel A, Guintard C, et al. (2017) Morphological integration in the appendicular skeleton of two domestic taxa: the horse and donkey. *Proc R Soc B* **284**, 20171241. doi:10.1098/rspb.2017.1241.

Hanot P, Herrel A, Guintard C, et al. (2018) The impact of artificial selection on morphological integration in the appendicular skeleton of domestic horses. *Journal of Anatomy* **232**, 657–673. doi:10.1111/joa.12772.

Hanot P, Herrel A, Guintard C, et al. (2019) Unravelling the hybrid vigor in domestic equids: the effect of hybridization on bone shape variation and covariation. *BMC Evol Biol* **19**, 1–13. doi:10.1186/s12862-019-1520-2.

Hildebrand M (1974) *Analysis of vertebrate structure*, New York: John Wiley & Sons.

Ho J, Tumkaya T, Aryal S, et al. (2019) Moving beyond P values: data analysis with estimation graphics. *Nat Methods* **16**, 565–566. doi:10.1038/s41592-019-0470-3.

Kelly EM, Sears KE (2011) Reduced phenotypic covariation in marsupial limbs and the implications for mammalian evolution. *Biol J Linn Soc* **102**, 22–36. doi:10.1111/j.1095-8312.2010.01561.x.

Klingenberg CP (2008) Morphological Integration and Developmental Modularity. *Annual Review of Ecology, Evolution, and Systematics* **39**, 115–132. doi:10.1146/annurev.ecolsys.37.091305.110054.

Klingenberg CP (2014) Studying morphological integration and modularity at multiple levels: concepts and analysis. *Philosophical Transactions of the Royal Society B: Biological Sciences* **369**, 20130249. doi:10.1098/rstb.2013.0249.

Klingenberg CP (2016) Size, shape, and form: concepts of allometry in geometric morphometrics. *Dev Genes Evol* **226**, 113–137. doi:10.1007/s00427-016-0539-2.

Lawler RR (2008) Morphological integration and natural selection in the postcranium of wild verreaux's sifaka (Propithecus verreauxi verreauxi). *American Journal of Physical Anthropology* **136**, 204–213. doi:10.1002/ajpa.20795.

Lessertisseur J, Saban R (1967) Le squelette. Squelette appendiculaire. In *Traité de Zoologie. Tome XVI, Fasicule 1: Mammifères.* Paris: Grassé Pierre-Paul, 298–1123.

Lord E, Pathmanathan JS, Corel E, et al. (2019) Introducing Trait Networks to Elucidate the Fluidity of Organismal Evolution Using Palaeontological Data. *Genome Biol Evol* **11**, 2653–2665. doi:10.1093/gbe/evz182.

Mallet C, Cornette R, Billet G, et al. (2019) Interspecific variation in the limb long bones among modern rhinoceroses—extent and drivers. *PeerJ* **7**, e7647. doi:10.7717/peerj.7647.

Mallison H, Wings O (2014) Photogrammetry in Paleontology - A practical guide. *Journal of Paleontological Techniques*, 1–31.

Martín-Serra A, Benson RBJ (2019) Developmental constraints do not influence long-term phenotypic evolution of marsupial forelimbs as revealed by interspecific disparity and integration patterns. *The American Naturalist*. doi:10.1086/707194.

Martín-Serra A, Figueirido B, Pérez-Claros JA, et al. (2015) Patterns of morphological integration in the appendicular skeleton of mammalian carnivores. *Evolution* **69**, 321–340. doi:10.1111/evo.12566.

McHorse BK, Biewener AA, Pierce SE (2019) The Evolution of a Single Toe in Horses: Causes, Consequences, and the Way Forward. *Integr Comp Biol* **59**, 638–655. doi:10.1093/icb/icz050.

Olson EC, Miller RL (1958) *Morphological Integration*, University of Chicago Press.

Owen R (1848) *On the Archetype and Homologies of the Vertebrate Skeleton*, London: John Van Voorst.

R Core Team (2014) *R: a language and environment for statistical computing*, Vienna: R Foundation for Statistical Computing.

Raia P, Carotenuto F, Passaro F, et al. (2012) Ecological Specialization in Fossil Mammals Explains Cope's Rule. *The American Naturalist* **179**, 328–337. doi:10.1086/664081.

Randau M, Goswami A (2018) Shape Covariation (or the Lack Thereof) Between Vertebrae and Other Skeletal Traits in Felids: The Whole is Not Always Greater than the Sum of Parts. *Evol Biol* **45**, 1–15. doi:10.1007/s11692-017-9443-6.

Regnault S, Hermes R, Hildebrandt T, et al. (2013) Osteopathology in the feet of rhinoceroses: lesion type and distribution. *Journal of Zoo and Wildlife Medicine* **44**, 918–927. doi:10.1638/2012-0277R1.1.

Rohlf FJ, Corti M (2000) Use of Two-Block Partial Least-Squares to Study Covariation in Shape. *Syst Biol* **49**, 740–753. doi:10.1080/106351500750049806.

Rohlf FJ, Slice D (1990) Extensions of the Procrustes Method for the Optimal Superimposition of Landmarks. *Syst Biol* **39**, 40–59. doi:10.2307/2992207.

Schlager S (2017) Chapter 9 - Morpho and Rvcg – Shape Analysis in R: R-Packages for Geometric Morphometrics, Shape Analysis and Surface Manipulations. In G. Zheng, S. Li, & G. Székely, eds. *Statistical Shape and Deformation Analysis*. Academic Press, 217–256. doi:10.1016/B978-0-12-810493-4.00011-0.

Schmidt M, Fischer MS (2009) Morphological Integration in Mammalian Limb Proportions: Dissociation Between Function and Development. *Evolution* **63**, 749–766. doi:10.1111/j.1558-5646.2008.00583.x.

Sears KE, Behringer RR, Rasweiler IV JJ, et al. (2007) The Evolutionary and Developmental Basis of Parallel Reduction in Mammalian Zeugopod Elements. *The American Naturalist* **169**, 105–117. doi:10.1086/510259.

Sears KE, Capellini TD, Diogo R (2015) On the serial homology of the pectoral and pelvic girdles of tetrapods. *Evolution* **69**, 2543–2555. doi:10.1111/evo.12773.

Streiner DL, Norman GR (2011) Correction for Multiple Testing: Is There a Resolution? *Chest* **140**, 16–18. doi:10.1378/chest.11-0523.

Van Valen L (1965) The Study of Morphological Integration. *Evolution* **19**, 347–349. doi:10.1111/j.1558-5646.1965.tb01725.x.

Wasserstein RL, Schirm AL, Lazar NA (2019) Moving to a World Beyond "p < 0.05." *The American Statistician* **73**, 1–19. doi:10.1080/00031305.2019.1583913.

Wiley DF, Amenta N, Alcantara DA, et al. (2005) Evolutionary Morphing. In *Proceedings of IEEE Visualization 2005*. Minneapolis, Minnesota.

Willerslev E, Gilbert MTP, Binladen J, et al. (2009) Analysis of complete mitochondrial genomes from extinct and extant rhinoceroses reveals lack of phylogenetic resolution. *BMC Evolutionary Biology* **9**, 1–11. doi:10.1186/1471-2148-9-95.

Wyman J (1867) On Symmetry and Homology in Limbs. *Proceedings of the Boston Society of Natural History* **9**, 1–45.

Young NM, Hallgrímsson B (2005) Serial Homology and the Evolution of Mammalian Limb Covariation Structure. *Evolution* **59**, 2691–2704. doi:10.1111/j.0014-3820.2005.tb00980.x.

Young NM, Wagner GP, Hallgrímsson B (2010) Development and the evolvability of human limbs. *PNAS* **107**, 3400–3405. doi:10.1073/pnas.0911856107.

Zelditch ML, Swiderski DL, Sheets HD, et al. (2012) *Geometric morphometrics for biologists: A Primer* Second Edition., Academic Press.

Zschokke S, Baur B (2002) Inbreeding, outbreeding, infant growth, and size dimorphism in captive Indian rhinoceros (Rhinoceros unicornis). *Can J Zool* **80**, 2014–2023. doi:10.1139/z02-183.

Figures

Figure 1: Graphic model showing the hypotheses of morphological integration tested in this study on the appendicular skeleton of the five modern rhino species. Hu: Humerus; Ra: Radius; Ul: Ulna; Fe: Femur; Ti: Tibia; Fi: Fibula.

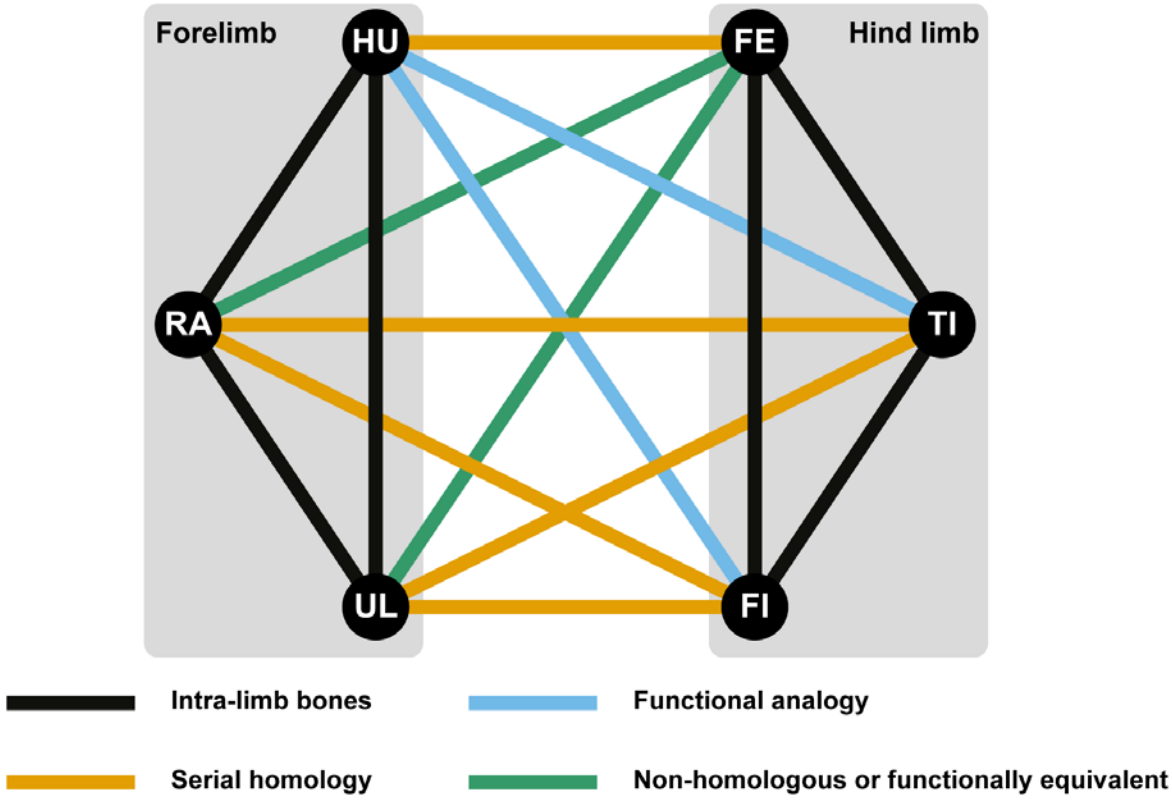

Figure 2: Plots of the first PLS axes computed on raw shapes. A: humerus-radius; B: humerus-ulna; C: humerus-femur; D: humerus-tibia; E: humerus-fibula; F: radius-ulna; G: radius-femur. rPLS: value of the PLS coefficient; % EC: percentage of explained covariation; Corr. p-value: corrected p-value using a Benjamini-Hochberg correction. The phylogenetic tree displays a polytomy because of the absence of consensus regarding the relationships of the five modern rhinos.

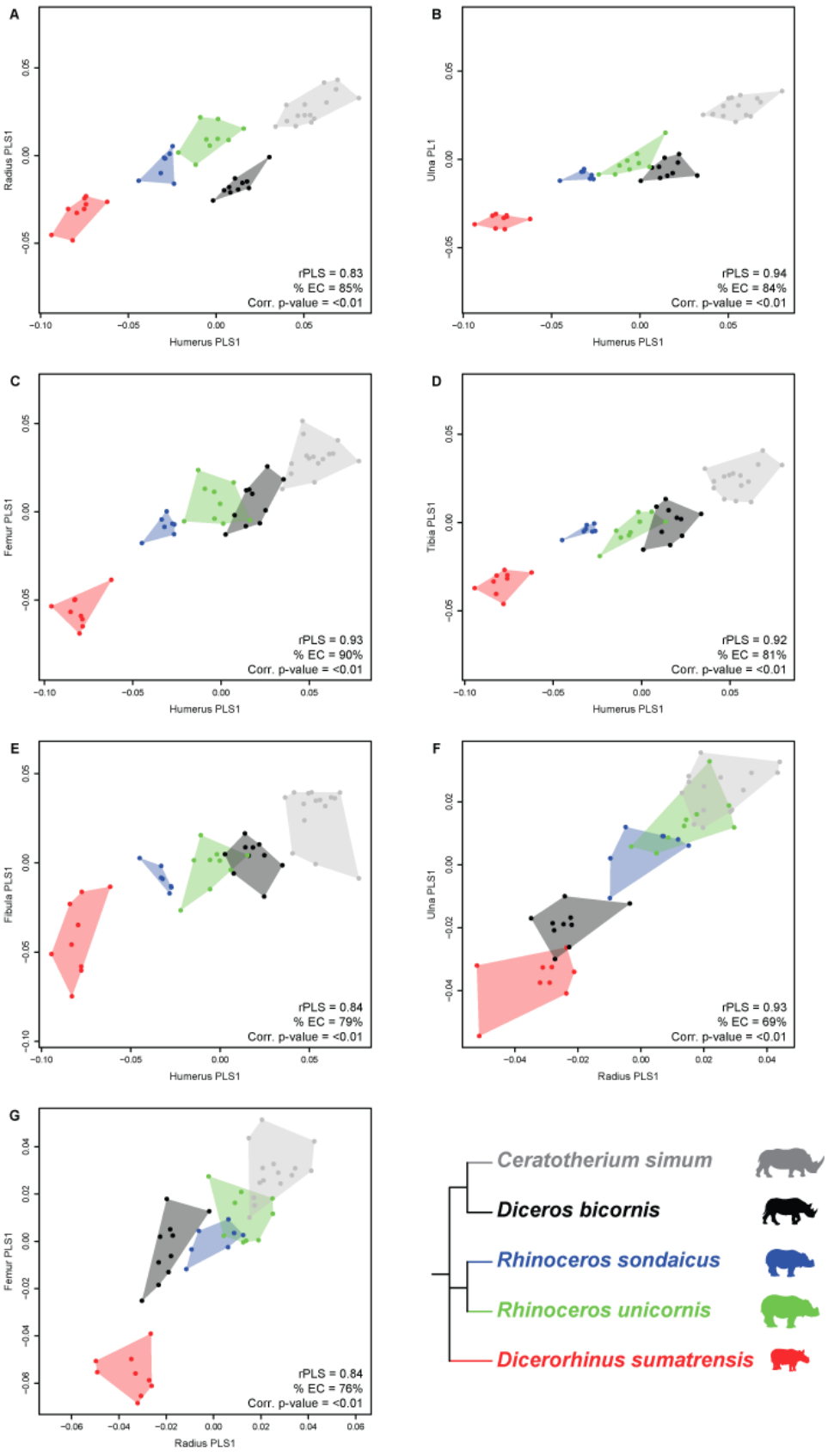
A
Radius PLS1
Humerus PLS1
rPLS = 0.83
% EC = 85%
Corr. p-value = <0.01
B
Ulna PL1
Humerus PLS1
rPLS = 0.94
% EC = 84%
Corr. p-value = <0.01
C
Femur PLS1
Humerus PLS1
rPLS = 0.93
% EC = 90%
Corr. p-value = <0.01
D
Tibia PLS1
Humerus PLS1
rPLS = 0.92
% EC = 81%
Corr. p-value = <0.01
E
Fibula PLS1
Humerus PLS1
rPLS = 0.84
% EC = 79%
Corr. p-value = <0.01
F
Ulna PLS1
Radius PLS1
rPLS = 0.93
% EC = 69%
Corr. p-value = <0.01
G
Femur PLS1
Radius PLS1
rPLS = 0.84
% EC = 76%
Corr. p-value = <0.01
Ceratotherium simum
Diceros bicornis
Rhinoceros sondaicus
Rhinoceros unicornis
Dicerorhinus sumatrensis

846

847

Figure 3: Plots of the first PLS axes computed on raw shapes. A: radius-tibia; B: radius-fibula; C: ulna-femur; D: ulna-tibia; E: ulna-fibula; F: femur-tibia; G: femur-fibula; H: tibia-fibula. rPLS: value of the PLS coefficient; % EC: percentage of explained covariation; Corr. p-value: corrected p-value using a Benjamini-Hochberg correction. Colour code as in Figure 2.

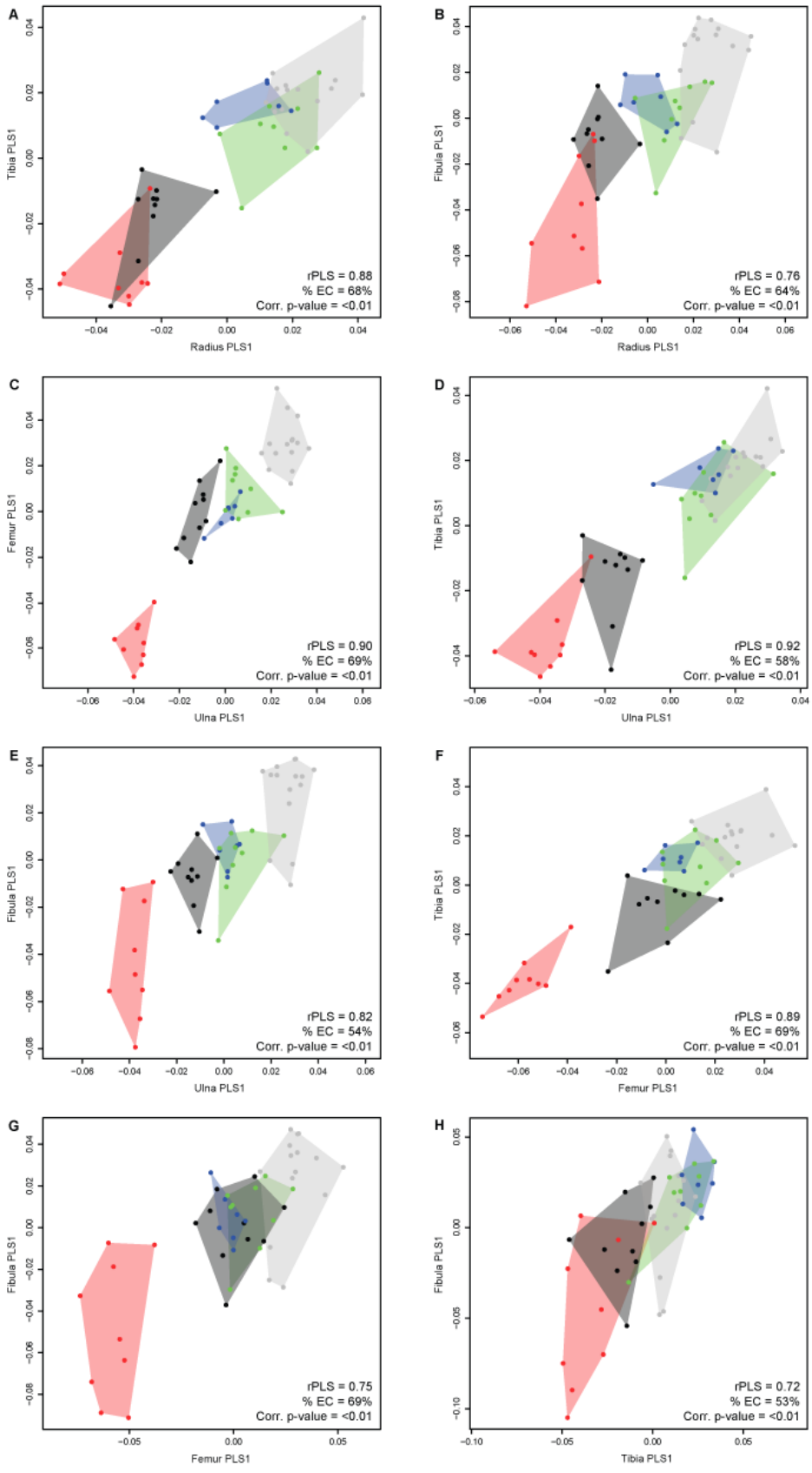
A
Tibia PLS1
Radius PLS1
rPLS = 0.88
% EC = 68%
Corr. p-value = <0.01
B
Fibula PLS1
Radius PLS1
rPLS = 0.76
% EC = 64%
Corr. p-value = <0.01
C
Femur PLS1
Ulna PLS1
rPLS = 0.90
% EC = 69%
Corr. p-value = <0.01
D
Tibia PLS1
Ulna PLS1
rPLS = 0.92
% EC = 58%
Corr. p-value = <0.01
E
Fibula PLS1
Ulna PLS1
rPLS = 0.82
% EC = 54%
Corr. p-value = <0.01
F
Tibia PLS1
Femur PLS1
rPLS = 0.89
% EC = 69%
Corr. p-value = <0.01
G
Fibula PLS1
Femur PLS1
rPLS = 0.75
% EC = 69%
Corr. p-value = <0.01
H
Fibula PLS1
Tibia PLS1
rPLS = 0.72
% EC = 53%
Corr. p-value = <0.01

852

853

Figure 4: Graphic model of the rPLS values of the first PLS axes computed on the appendicular skeleton of the five modern rhino species. The line thickness is proportional to the rPLS value. The colour code expresses the type of relation between bones as described in the Figure 1. A: rPLS values obtained on raw shapes. B: rPLS values obtained on allometry-free shapes. In brackets are indicated the percentages of difference between rPLS obtained on raw shapes and allometry-free shapes. Hu: Humerus; Ra: Radius; Ul: Ulna; Fe: Femur; Ti: Tibia; Fi: Fibula.

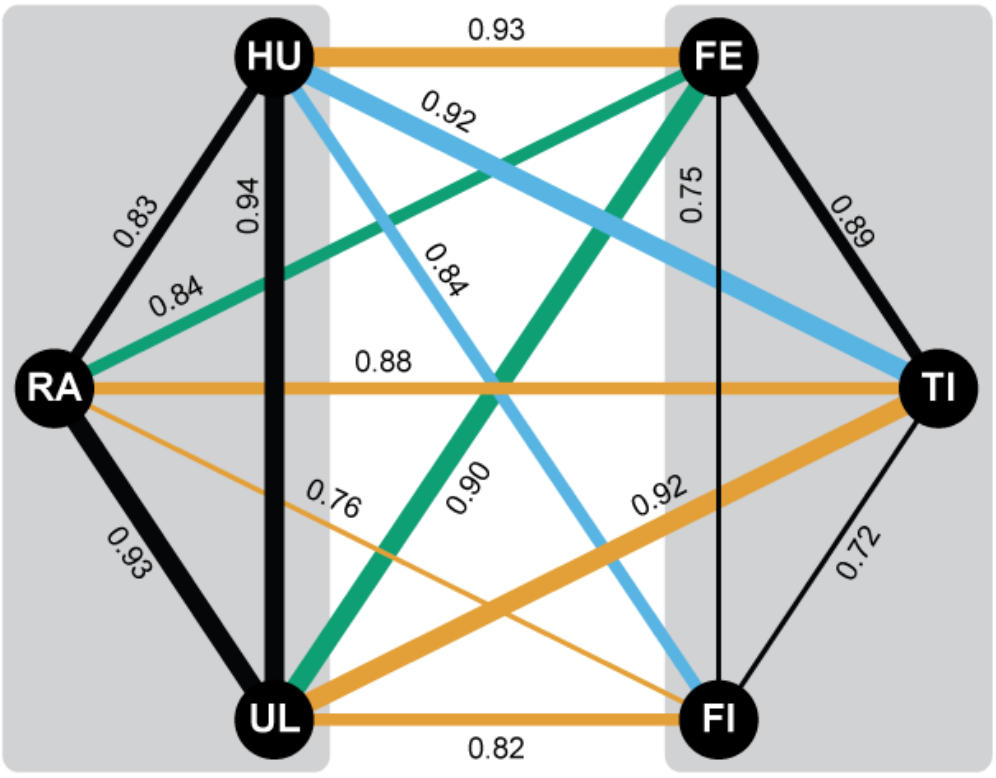
HU
FE
RA
TI
UL
FI
0.93
0.92
0.83
0.94
0.75
0.89
0.84
0.84
0.88
0.76
0.90
0.92
0.93
0.72
0.82

A

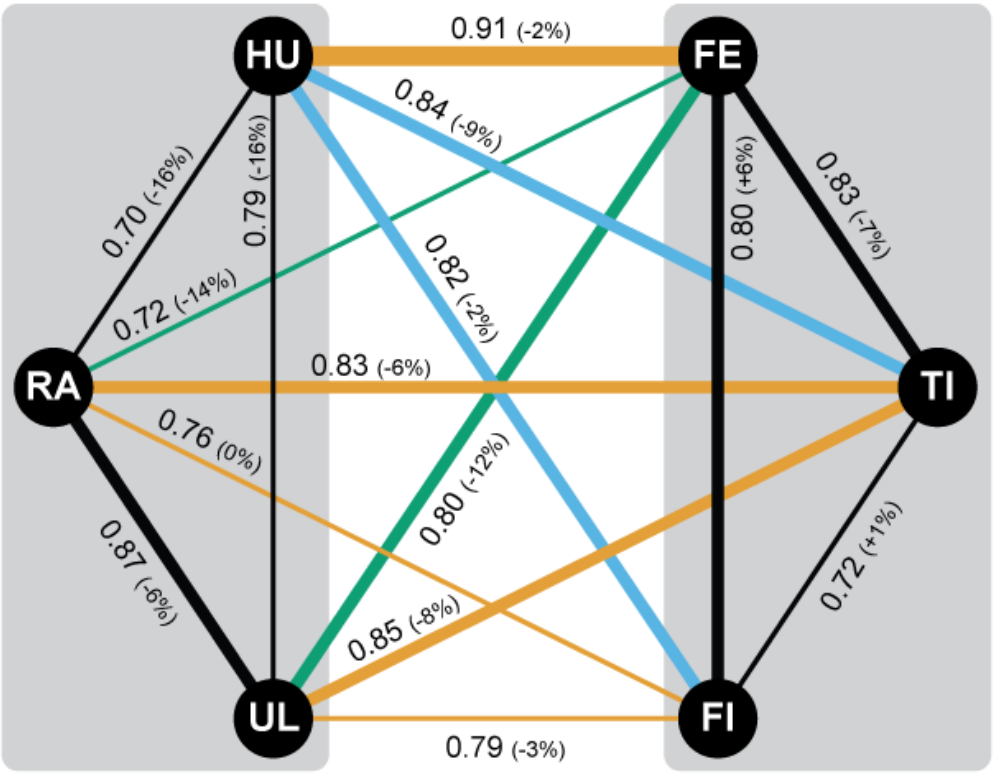
HU
FE
RA
TI
UL
FI
0.91 (-2%)
0.84 (-9%)
0.70 (-16%)
0.79 (-16%)
0.80 (+6%)
0.83 (-7%)
0.72 (-14%)
0.82 (-2%)
0.83 (-6%)
0.76 (0%)
0.80 (-12%)
0.87 (-6%)
0.85 (-8%)
0.72 (+1%)
0.79 (-3%)

B

860

861

Figure 5: Colour maps of the location and intensity of the shape deformation associated to the first PLS axes for 4 pairs of bones among the five modern species of rhinoceros. For each bone, the shape associated to the positive part of the first PLS axis was coloured depending on its distance to the shape associated to the negative part (blue indicates a low deformation intensity and red indicates a high deformation intensity). The colour code of the squares expresses the type of relation between bones as described in the Figure 1 (orange: serial homology; blue: functional analogy). A: humerus-femur; B: radius-tibia; C: ulna-fibula; D: humerus-tibia (orientation from left to right in each case: cranial, lateral, caudal and medial).

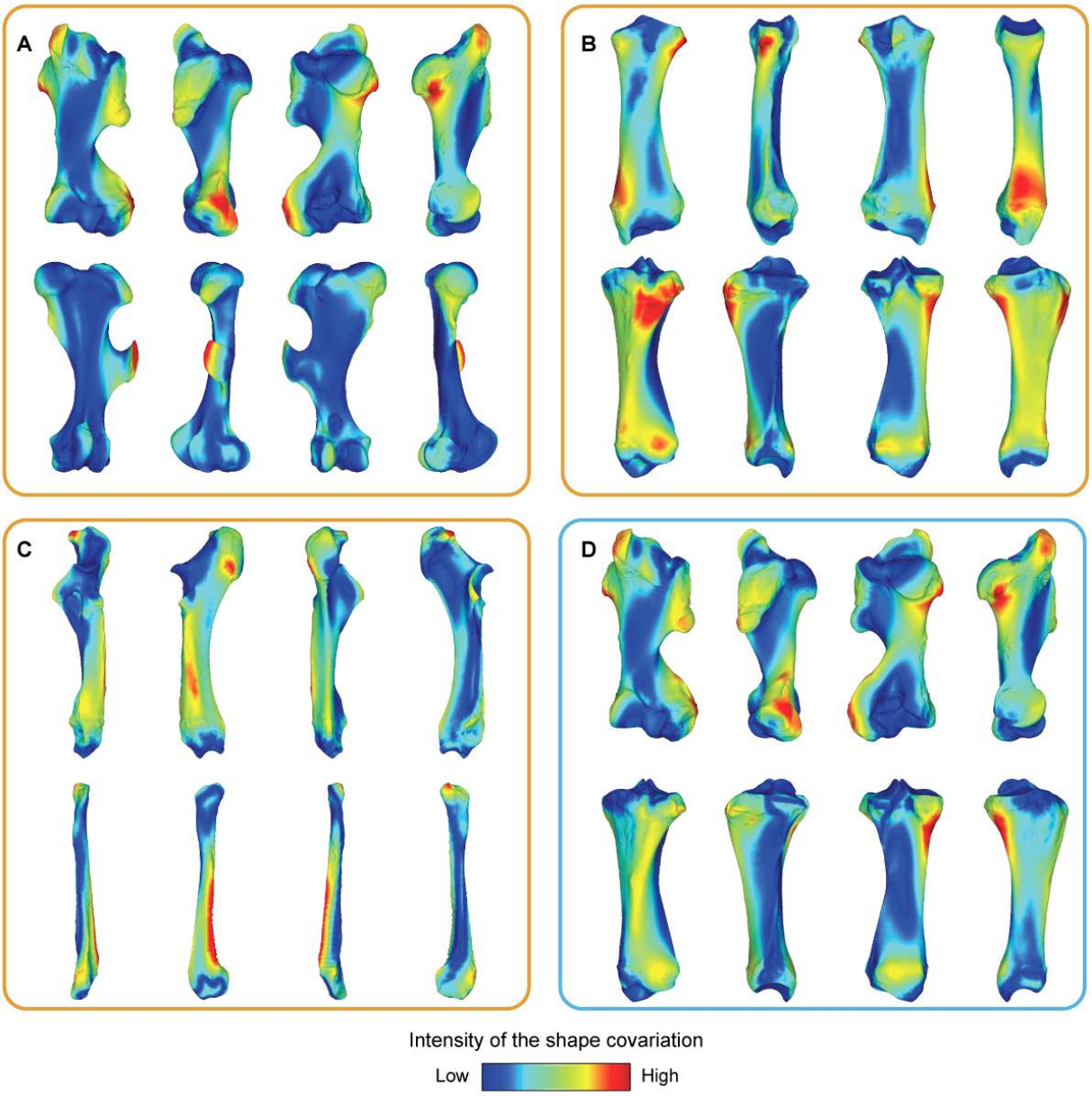

Figure 6: Colour maps of the location and intensity of the shape deformation associated to the first PLS axes for 4 pairs of bones among the five modern species of rhinoceros. For each bone, the shape associated to the positive part of the first PLS axis was coloured depending on its distance to the shape associated to the negative part (blue indicates a low deformation intensity and red indicate a high deformation intensity). The colour code of the squares expresses the type of relation between bones as described in the Figure 1 (black: intra-limb relation; green: non-homologous or analogous bones). A: radius-ulna; B: femur-tibia; C: tibia-fibula; D: ulna-femur (orientation from left to right in each case: cranial, lateral, caudal and medial).

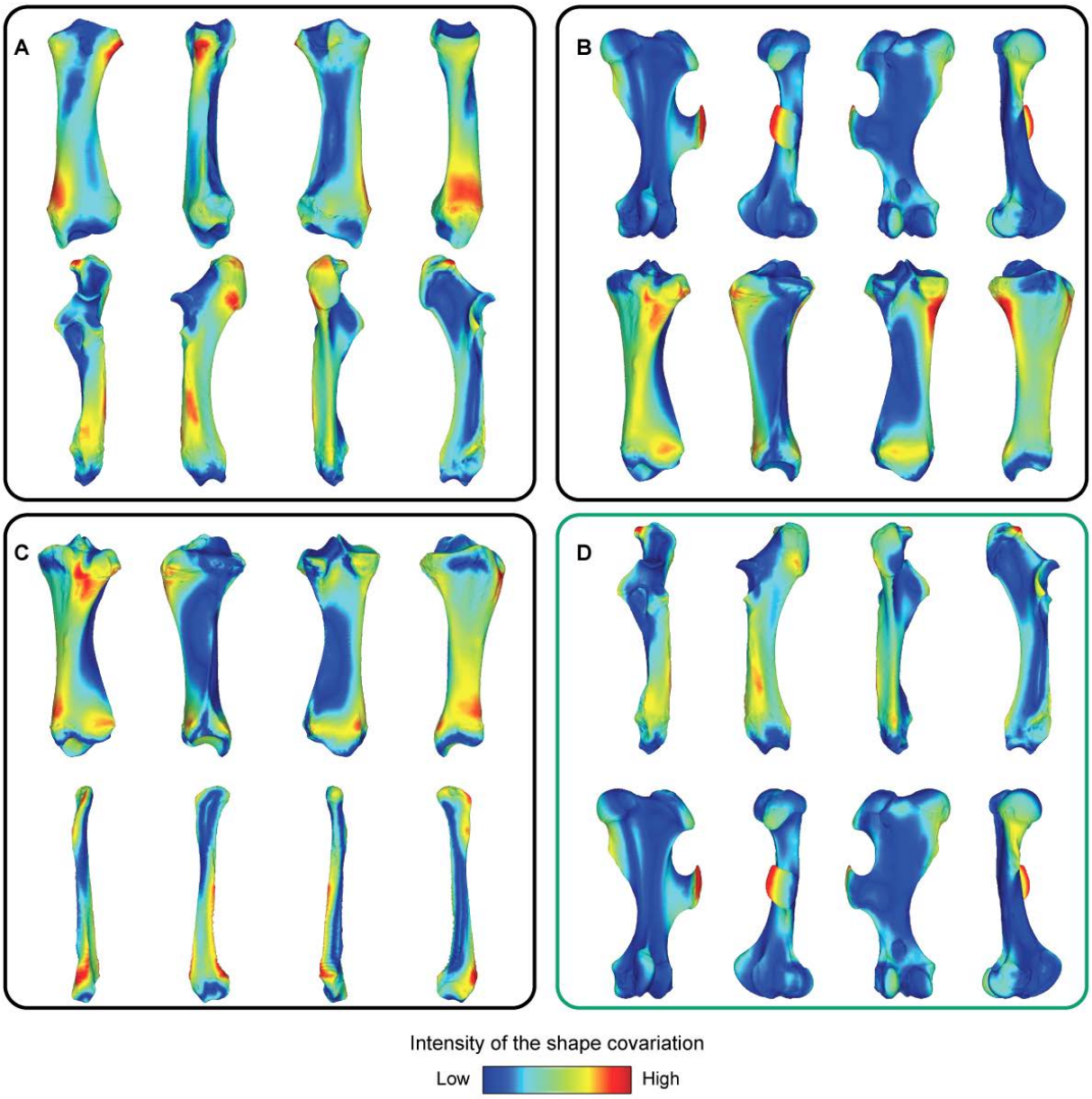

881 **Figure 7:** Plots of the first PLS axes computed on allometry-free shapes. A: humerus-radius; B: humerus-
882 ulna; C: humerus-femur; D: humerus-tibia; E: humerus-fibula; F: radius-ulna; G: radius-femur. rPLS: value
883 of the PLS coefficient; % EC: percentage of explained covariation; Corr. p-value: corrected p-value using a
884 Benjamini-Hochberg correction. The phylogenetic tree displays a polytomy because of the absence of
885 consensus regarding the relationships of the five modern rhinos.

886

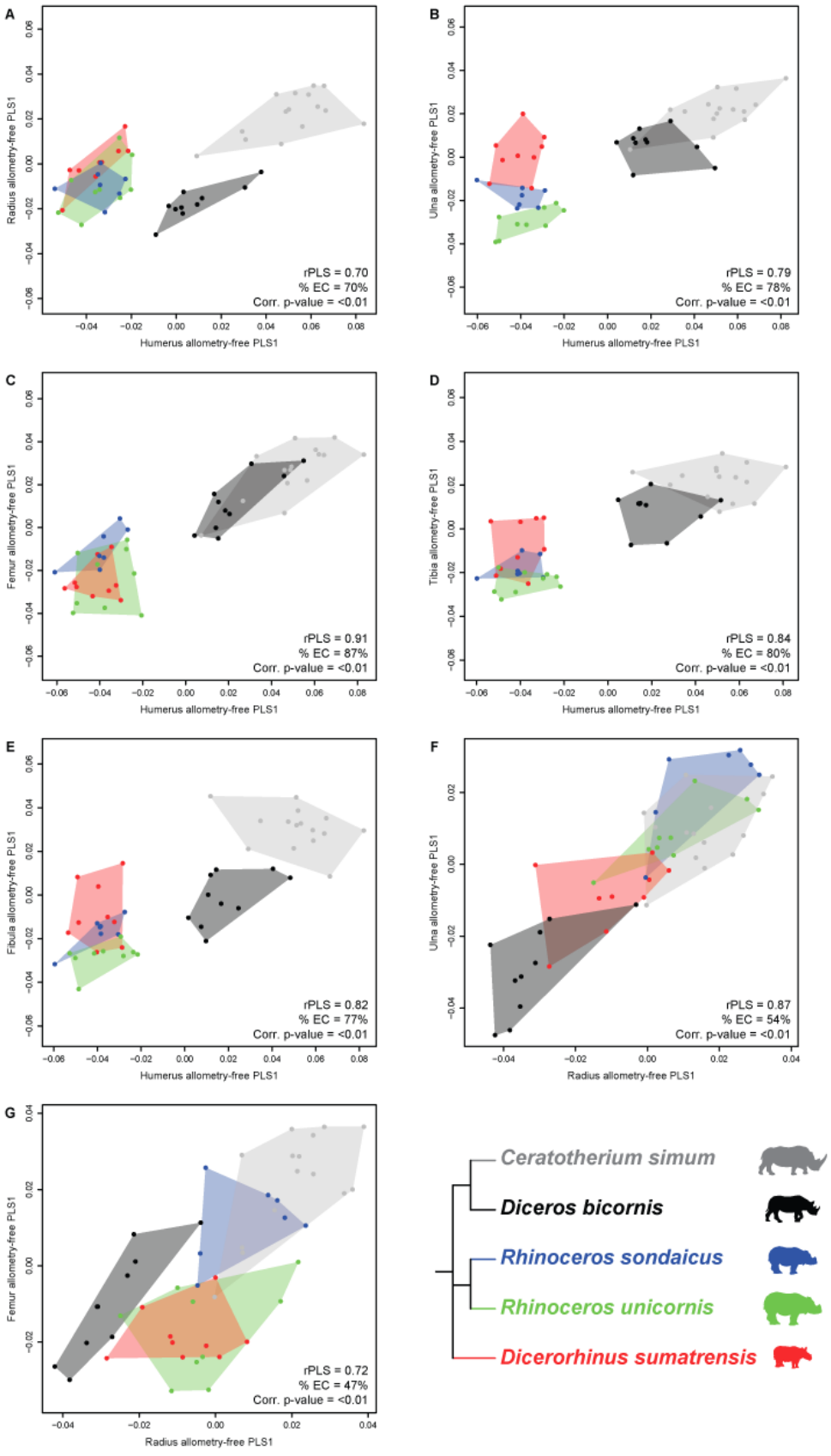
A
Radius allometry-free PLS1
Humerus allometry-free PLS1
rPLS = 0.70
% EC = 70%
Corr. p-value = <0.01
B
Ulna allometry-free PLS1
Humerus allometry-free PLS1
rPLS = 0.79
% EC = 78%
Corr. p-value = <0.01
C
Femur allometry-free PLS1
Humerus allometry-free PLS1
rPLS = 0.91
% EC = 87%
Corr. p-value = <0.01
D
Tibia allometry-free PLS1
Humerus allometry-free PLS1
rPLS = 0.84
% EC = 80%
Corr. p-value = <0.01
E
Fibula allometry-free PLS1
Humerus allometry-free PLS1
rPLS = 0.82
% EC = 77%
Corr. p-value = <0.01
F
Ulna allometry-free PLS1
Radius allometry-free PLS1
rPLS = 0.87
% EC = 54%
Corr. p-value = <0.01
G
Femur allometry-free PLS1
Radius allometry-free PLS1
rPLS = 0.72
% EC = 47%
Corr. p-value = <0.01
Ceratotherium simum
Diceros bicornis
Rhinoceros sondaicus
Rhinoceros unicornis
Dicerorhinus sumatrensis

887

888 **Figure 8:** Plots of the first PLS axes computed on allometry-free shapes. A: radius-tibia; B: radius-fibula;
889 C: ulna-femur; D: ulna-tibia; E: ulna-fibula; F: femur-tibia; G: femur-fibula; H: tibia-fibula. rPLS: value of
890 the PLS coefficient; % EC: percentage of explained covariation; Corr. p-value: corrected p-value using a
891 Benjamini-Hochberg correction. Colour code as in Figure 6.

892

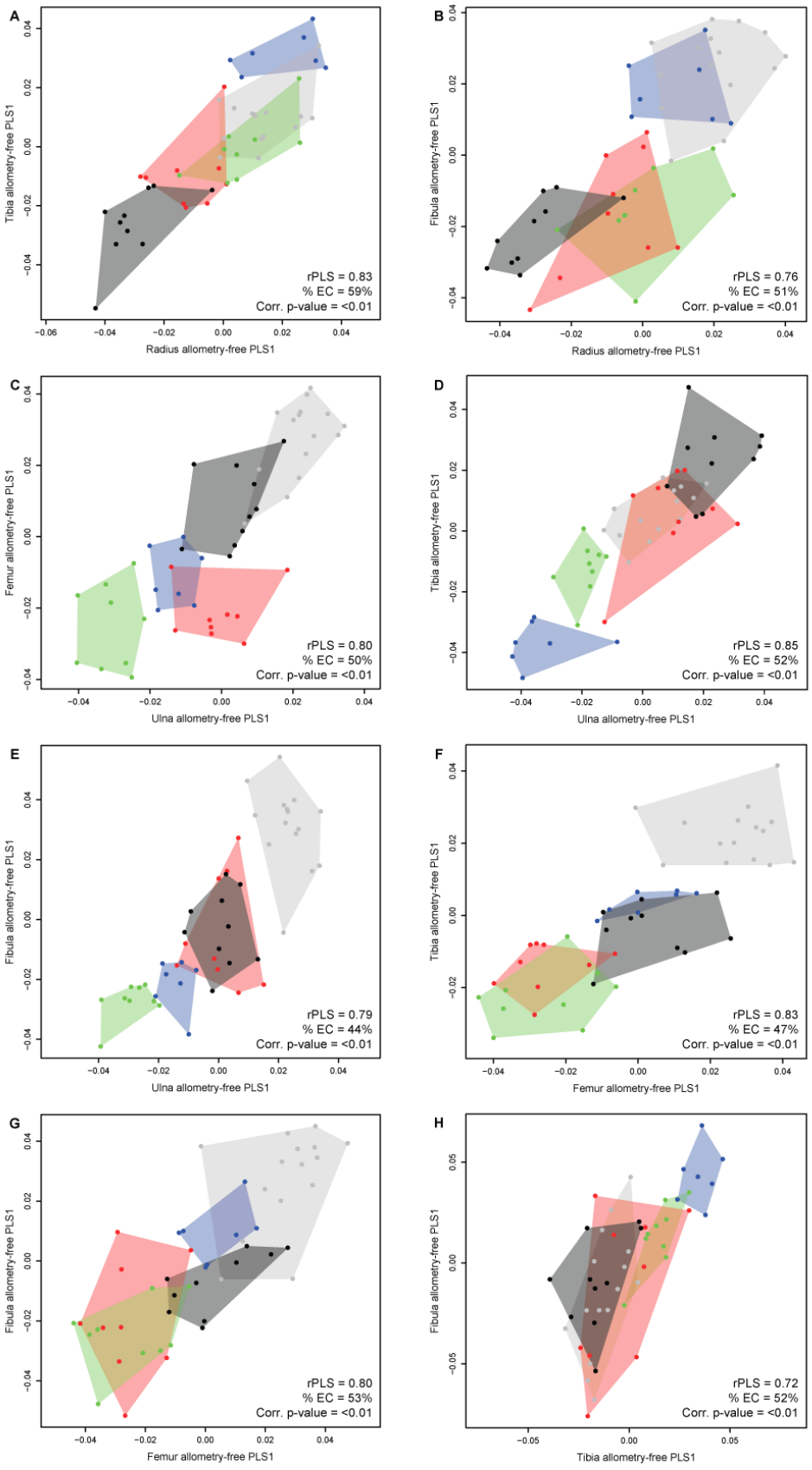
A
Tibia allometry-free PLS1
Radius allometry-free PLS1
rPLS = 0.83
% EC = 59%
Corr. p-value = <0.01
B
Fibula allometry-free PLS1
Radius allometry-free PLS1
rPLS = 0.76
% EC = 51%
Corr. p-value = <0.01
C
Femur allometry-free PLS1
Ulna allometry-free PLS1
rPLS = 0.80
% EC = 50%
Corr. p-value = <0.01
D
Tibia allometry-free PLS1
Ulna allometry-free PLS1
rPLS = 0.85
% EC = 52%
Corr. p-value = <0.01
E
Fibula allometry-free PLS1
Ulna allometry-free PLS1
rPLS = 0.79
% EC = 44%
Corr. p-value = <0.01
F
Tibia allometry-free PLS1
Femur allometry-free PLS1
rPLS = 0.83
% EC = 47%
Corr. p-value = <0.01
G
Fibula allometry-free PLS1
Femur allometry-free PLS1
rPLS = 0.80
% EC = 53%
Corr. p-value = <0.01
H
Fibula allometry-free PLS1
Tibia allometry-free PLS1
rPLS = 0.72
% EC = 52%
Corr. p-value = <0.01

893

Figure 9: Plots of the first PLS axes computed on the 15 *Ceratotherium simum* specimens. Adults are highlighted in light grey and subadults in dark grey. The size of the dots is proportional to the combined value of the centroid size of the bones for each block and each specimen. A: humerus-radius; B: humerus-femur; C: radius-femur; D: ulna-femur. Sex: F: female; M: male; U: unknown; rPLS: value of the PLS coefficient; % EC: percentage of explained covariation; Corr. p-value: corrected p-value using a Benjamini-Hochberg correction.

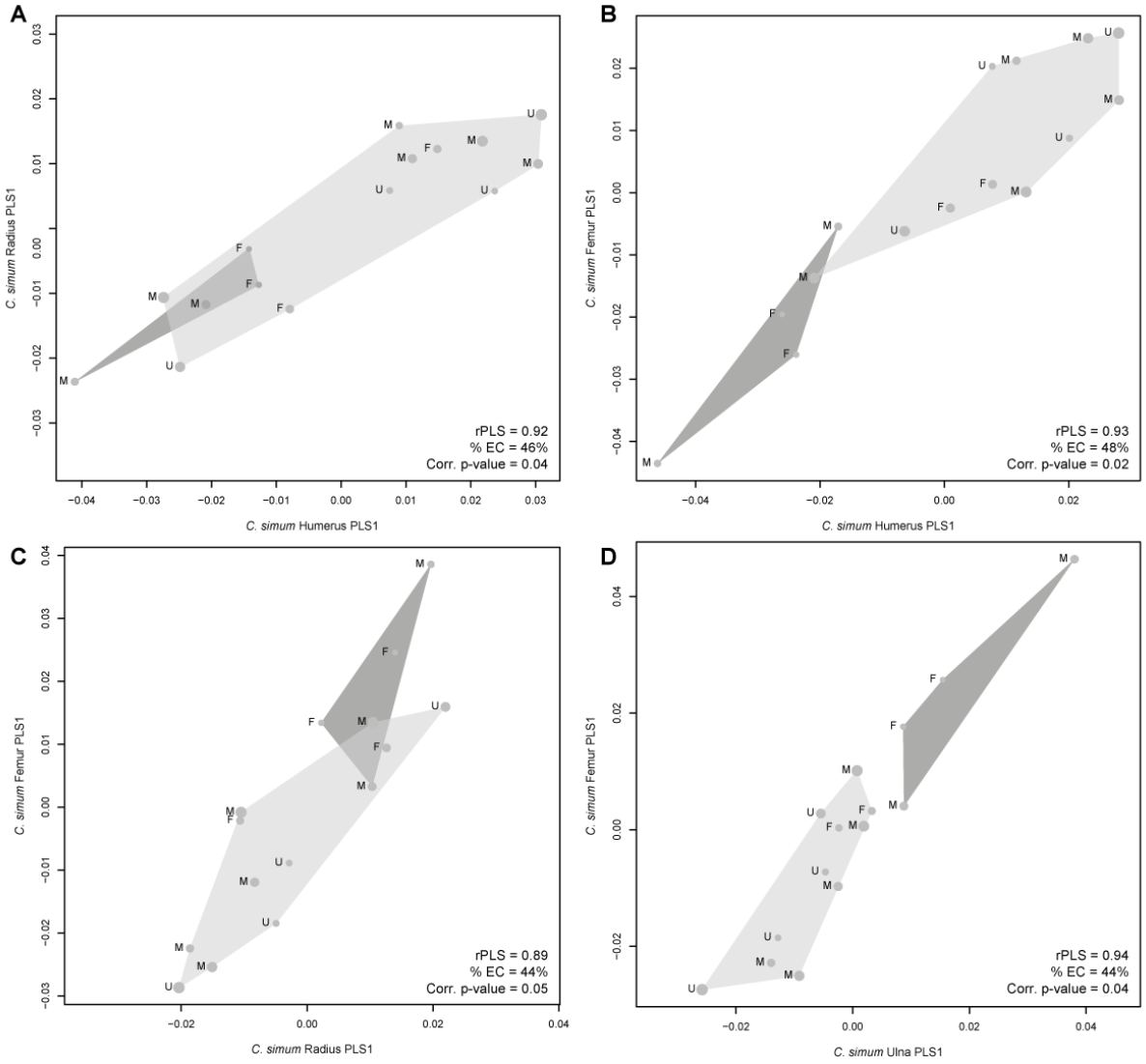

Figure 10: Colour maps of the location and intensity of the shape deformation associated to the first PLS axes for four bones of *Ceratotherium simum*. For each bone, the shape associated to the positive part of the first PLS axis was coloured depending on its distance to the shape associated to the negative part (blue indicates a low deformation intensity and red indicates a high deformation intensity). The colour code of the squares expresses the type of relation between bones as described in the Figure 1 (black: intra-limb relation; orange: serial homology; green: non-homologous or analogous bones). A: humerus-radius; B: humerus-femur; C: radius-femur; D: ulna-femur (orientation from left to right in each case: cranial, lateral, caudal and medial).

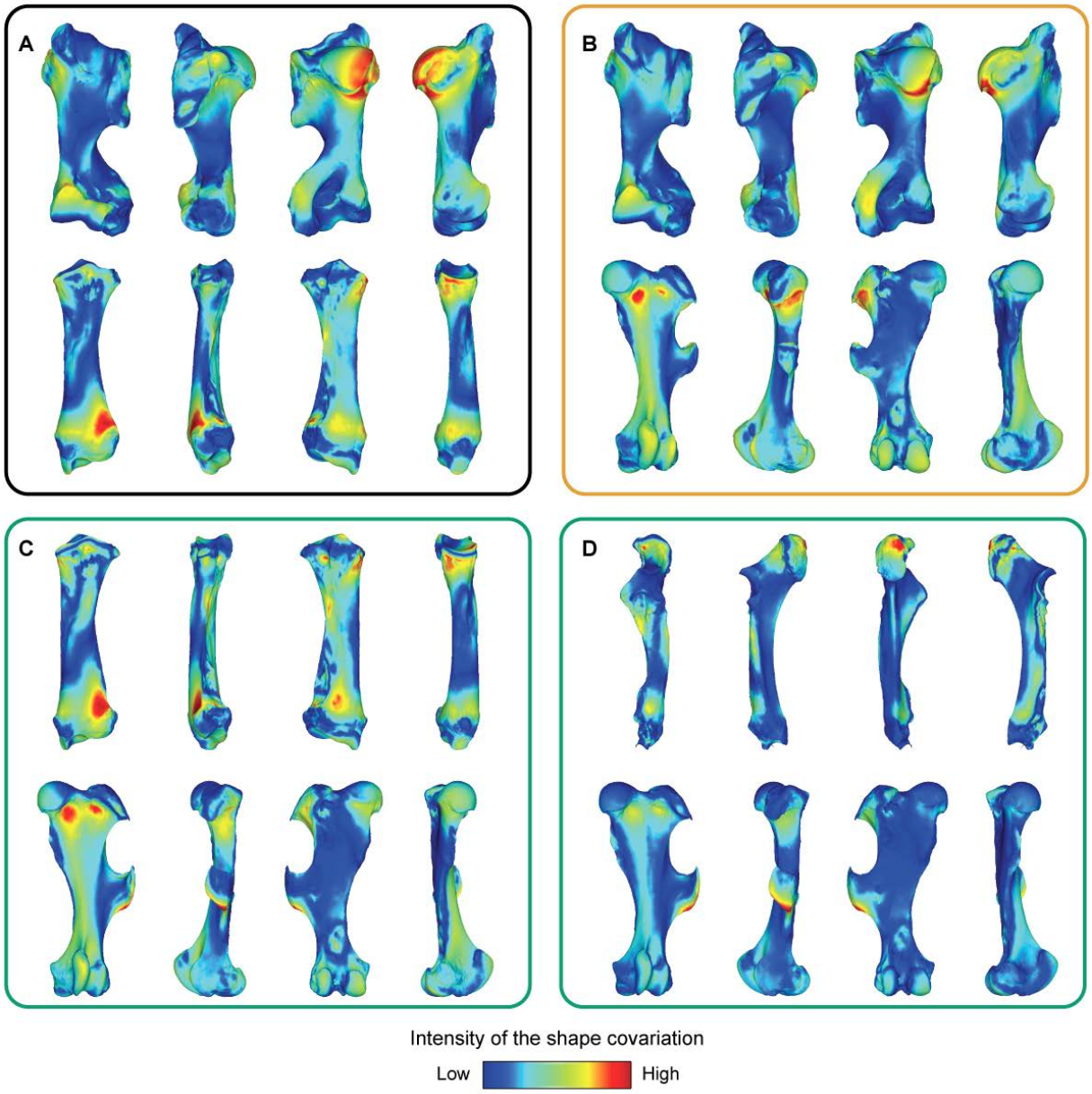

Tables

Table 1: List of the studied specimens with sex, age class, condition and 3D acquisition details. Abbreviations: Sex: F: female; M: male; U: unknown. Age – A: adult; S: sub-adult. Condition – W: wild; C: captive; U: unknown. 3D acquisition – SS: surface scanner; P: photogrammetry. Institutional abbreviations: AMNH: American Museum of Natural History, New York. BICPC: Powell Cotton Museum, Birchington-on-Sea. CCEC: Centre de Conservation et d'Étude des Collections, Musée des Confluences, Lyon. MNHN: Muséum National d'Histoire Naturelle, Paris. NHMUK: Natural History Museum, London. NHMW: Naturhistorisches Museum Wien, Vienna. RBINS: Royal Belgian Institute of Natural Sciences, Brussels. RMCA: Royal Museum for Central Africa, Tervuren. ZSM: Zoologische Staatssammlung München, Munich. Specimens MNHN-ZM-AC-1885-734, NHMUK ZD 2018.143 and NHMUK ZD 1972.822 were previously determined or reattributed based on the analysis of the limb long bone morphology (see Mallet et al. 2019).

Taxon	Institution	Specimen number	Sex	Age	Condition	3D acquisition
Ceratotherium simum	AMNH	M-51854	F	A	W	SS
Ceratotherium simum	AMNH	M-51855	M	A	W	SS
Ceratotherium simum	AMNH	M-51857	F	A	W	SS
Ceratotherium simum	AMNH	M-51858	M	A	W	SS
Ceratotherium simum	AMNH	M-81815	U	A	U	SS
Ceratotherium simum	BICPC	NH.CON.20	M	S	W	SS
Ceratotherium simum	BICPC	NH.CON.32	F	S	W	SS
Ceratotherium simum	BICPC	NH.CON.40	F	S	W	SS
Ceratotherium simum	BICPC	NH.CON.110	M	A	W	SS
Ceratotherium simum	BICPC	NH.CON.112	M	A	W	SS
Ceratotherium simum	NHMUK	ZD 2018.143	U	A	U	SS
Ceratotherium simum	NHMW	3086	U	A	W	P
Ceratotherium simum	RBINS	19904	M	S	W	SS
Ceratotherium simum	RMCA	1985.32-M-0001	U	A	W	SS
Ceratotherium simum	RMCA	RG35146	M	A	W	SS
Dicerorhinus sumatrensis	MNHN	ZM-AC-1903-300	M	A	W	SS
Dicerorhinus sumatrensis	NHMUK	ZD 1879.6.14.2	M	A	W	SS
Dicerorhinus sumatrensis	NHMUK	ZD 1894.9.24.1	U	A	W	SS
Dicerorhinus sumatrensis	NHMUK	ZD 1931.5.28.1	M	S	W	SS
Dicerorhinus sumatrensis	NHMUK	ZE 1948.12.20.1	U	A	U	SS
Dicerorhinus sumatrensis	NHMUK	ZE 1949.1.11.1	U	A	W	SS
Dicerorhinus sumatrensis	NHMW	3082	U	A	U	P
Dicerorhinus sumatrensis	RBINS	1204	M	A	W	SS
Dicerorhinus sumatrensis	ZSM	1908/571	M	A	U	SS
Diceros bicornis	AMNH	M-81805	U	A	U	SS
Diceros bicornis	AMNH	M-27757	M	S	W	SS
Diceros bicornis	AMNH	M-113776	U	A	W	SS
Diceros bicornis	AMNH	M-113777	U	A	W	SS
Diceros bicornis	AMNH	M-113778	U	A	W	SS
Diceros bicornis	MNHN	ZM-AC-1936-644	F	S	U	SS
Diceros bicornis	RBINS	9714	F	A	W	SS
Diceros bicornis	RMCA	RG2133	M	S	W	SS
Diceros bicornis	ZSM	1961/186	M	S	U	SS
Diceros bicornis	ZSM	1961/187	M	S	U	SS
Rhinoceros sondaicus	CCEC	50002041	U	A	W	SS
Rhinoceros sondaicus	MNHN	ZM-AC-A7970	U	A	U	SS
Rhinoceros sondaicus	MNHN	ZM-AC-A7971	U	A	W	SS
Rhinoceros sondaicus	NHMUK	ZD 1861.3.11.1	U	S	W	SS
Rhinoceros sondaicus	NHMUK	ZD 1871.12.29.7	M	A	W	SS
Rhinoceros sondaicus	NHMUK	ZD 1921.5.15.1	F	S	W	SS
Rhinoceros sondaicus	RBINS	1205F	U	S	W	SS
Rhinoceros unicornis	AMNH	M-35759	M	A	C	SS
Rhinoceros unicornis	AMNH	M-54456	F	A	W	SS
Rhinoceros unicornis	MNHN	ZM-AC-1960-59	M	A	C	SS
Rhinoceros unicornis	NHMUK	ZD 1884.1.22.1.2	F	A	W	SS
Rhinoceros unicornis	NHMUK	ZE 1950.10.18.5	M	A	W	SS
Rhinoceros unicornis	NHMUK	ZE 1961.5.10.1	M	A	W	SS
Rhinoceros unicornis	NHMUK	ZD 1972.822	U	A	U	SS
Rhinoceros unicornis	RBINS	1208	F	A	C	SS
Rhinoceros unicornis	RBINS	33382	U	A	U	SS

924

925 **Table 2:** Values of the rPLS for the first PLS axes for each of the five species, with respective p-values before (p) and after (p cor.) the Benjamini-
926 Hochberg correction. Values in bold are the statistically significant ones (p or p cor. < 0.05). Abbreviations: Hum: Humerus: Rad: Radius; Uln:
927 Ulna; Fem: Femur; Tib: Tibia; Fib: Fibula.

		***C. simum* (n=15)**			***Ds. sumatrensis* (n=9)**			***Dc. bicornis* (n=10)**			***R. sondaicus* (n=7)**			***R. unicornis* (n=9)**		
	Paired bones	**rPLS**	**p**	**p cor.**	**rPLS**	**p**	**p cor.**	**rPLS**	**p**	**p cor.**	**rPLS**	**p**	**p cor.**	**rPLS**	**p**	**p cor.**
Intra-limb bones	Hum-Rad	**0.92**	**0.01**	**0.04**	0.85	0.40	0.59	0.89	0.19	0.55	**0.98**	**0.01**	0.10	0.90	0.37	0.59
	Hum-Uln	**0.91**	**0.04**	0.11	0.96	0.24	0.49	0.91	0.38	0.59	0.98	0.17	0.23	**0.93**	**0.04**	0.25
	Rad-Uln	0.88	0.07	0.16	0.91	0.28	0.49	0.96	0.11	0.55	0.97	0.09	0.15	0.95	0.48	0.59
	Fem-Tib	0.85	0.25	0.36	0.88	0.27	0.49	0.92	0.14	0.55	0.97	0.09	0.15	0.79	0.54	0.59
	Fem-Fib	0.78	0.87	0.87	0.87	0.95	0.95	0.87	0.29	0.55	0.95	0.26	0.30	0.84	0.55	0.59
	Tib-Fib	0.72	0.12	0.26	0.68	0.30	0.49	0.80	0.73	0.92	0.98	0.08	0.15	**0.95**	**0.01**	0.11
Serial homology	Hum-Fem	**0.93**	**0.01**	**0.02**	**0.95**	**0.02**	0.15	0.91	0.59	0.80	0.97	0.30	0.30	0.93	0.21	0.59
	Rad-Tib	0.90	0.27	0.36	0.70	0.77	0.95	0.94	0.23	0.55	**0.98**	**0.03**	0.10	0.93	0.51	0.59
	Rad-Fib	0.73	0.26	0.36	0.66	0.85	0.95	0.76	0.81	0.55	**0.95**	**0.05**	0.15	0.87	0.64	0.64
	Uln-Tib	0.84	0.36	0.41	0.92	0.29	0.49	**0.94**	**0.05**	0.55	0.97	0.09	0.15	**0.91**	**0.05**	0.25
	Uln-Fib	0.76	0.34	0.41	0.93	0.90	0.95	0.89	0.99	0.99	0.97	0.27	0.30	0.90	0.14	0.54
Functional equivalence	Hum-Tib	0.90	0.17	0.33	**0.93**	**0.01**	0.15	0.86	0.21	0.55	**0.99**	**0.01**	0.10	0.96	0.26	0.59
	Hum-Fib	0.77	0.65	0.69	0.80	0.63	0.85	0.90	0.81	0.93	0.95	0.11	0.16	0.91	0.48	0.59
Non-homologous or functionally equivalent	Rad-Fem	**0.89**	**0.01**	**0.05**	0.89	0.07	0.33	0.89	0.40	0.59	0.96	0.29	0.30	0.80	0.36	0.59
	Uln-Fem	**0.94**	**0.01**	**0.04**	0.93	0.19	0.49	0.89	0.86	0.93	**0.98**	**0.02**	0.10	0.97	0.37	0.59

928

Supporting Information

Figure S1: Summary of the anatomical areas of the rhino long bone. Bones figured here belong to *C. simum*. **A: Humerus. Abbreviations** – B.g.: Bicipital groove; C.: Capitulum; D.t.: Deltoid tuberosity; E.c.: Epicondylar crest; G.t.: Greater tubercle; G.t.c.: Greater tubercle convexity; H.: Head; I.t.: Intermediate tubercle; L.e.: Lateral epicondyle; L.l.b.: Lateral lip border; L.t.: Lesser tubercle; L.t.c.: Lesser tubercle convexity; M.e.: Medial epicondyle; M.i.i.: M. infraspinatus insertion; M.l.b.: Medial lip border; M.t.m.t.: M. teres major tuberosity; N.: Neck; O.f.: Olecranon fossa; T.: Trochlea; T.g.: Trochlear groove. **B: Radius. Abbreviations** – A.s.s.: Articular surface for the scaphoid; A.s.sl.: Articular surface for the semilunar; C.p.: Coronoid process; D.a.s.u.: Distal articular surface for the ulna; I.c.: Interosseous crest; I.s.: Interosseous space; L.g.c.: Lateral glenoid cavity; L.i.r.: Lateral insertion relief; L.s.a.s.: Lateral synovial articular surface; M.g.c.: Medial glenoid cavity; M.s.a.s.: Medial synovial articular surface; P.a.s.u.: Proximal articular surface for the ulna; P.p.: Palmar process; R.s.p.: Radial styloid process; R.t.: Radial tuberosity. **C: Ulna. Abbreviations** – A.p.: Anconeal process; A.s.h.: Articular surface for the humerus; A.s.p.: Articular surface for the pisiform; A.s.sl.: Articular surface for the semilunar; A.s.t.: Articular surface for the triquetrum; D.a.s.r.: Distal articular surface for the radius; I.c.: Interosseous crest; I.s.: Interosseous space; M.t.o.: Medial tuberosity of the olecranon; O.t.: Olecranon tuberosity; P.b.: palmar border; U.s.p.: Ulnar styloid process. **D: Femur. Abbreviations** – F.c.: Fovea capitis; G.t.: Greater trochanter; G.t.c.: Greater trochanter convexity; G.t.t.: Greater trochanter top; H.: Head; I.s.: Intercondylar space; L.c.: Lateral condyle; L.e.: Lateral epicondyle; L.t.r.: Lateral trochlear ridge; L.t.: Lesser trochanter; M.c.: Medial condyle; M.e.: Medial epicondyle; M.t.r.: Medial trochlear ridge; N.: Neck; S.f.: supracondylar fossa; T.: Trochlea; T.f.: Trochanteric fossa; T.g.: Trochlear groove; T.t.: Third trochanter. **E: Tibia. Abbreviations** – A.s.t.: Articular surface for the talus; C.a.: Caudal apophysis; Ce.i.a.: Central intercondylar area; Cr.i.a.: Cranial intercondylar area; D.a.s.f.: Distal articular surface for the fibula; E.g.: Extensor groove; I.c.: Interosseous crest; L.a.s.: Lateral articular surface; L.c.: Lateral condyle; L.g.: Lateral groove; L.i.t.: Lateral intercondylar tubercle; M.a.s.: Medial articular surface; M.c.: Medial condyle; M.g.: Medial groove; M.i.t.: Medial intercondylar tubercle; M.m.: Medial malleolus; P.a.s.f.: Proximal articular surface for the fibula; P.n.: Popliteal notch; S.s.m.p.: Sliding surface for the m. popliteus; T.c.: Tibial crest; T.g.: Tuberosity groove; T.t.: Tibial tuberosity. **F: Fibula. Abbreviations** – A.s.t.: Articular surface for the talus; Ca.l.: Caudo-lateral line; Ca.t.l.m.: Caudal tubercle of the lateral malleolus; Cr.l.: Cranio-lateral line; Cr.t.l.m.: Cranial tubercle of the lateral malleolus; D.a.s.t.: Distal articular surface for the tibia; D.g.m.: Distal groove of the malleolus; H.: Head; I.c.: Interosseous crest; L.g.: Lateral groove; P.a.s.t.: Proximal articular surface for the tibia.

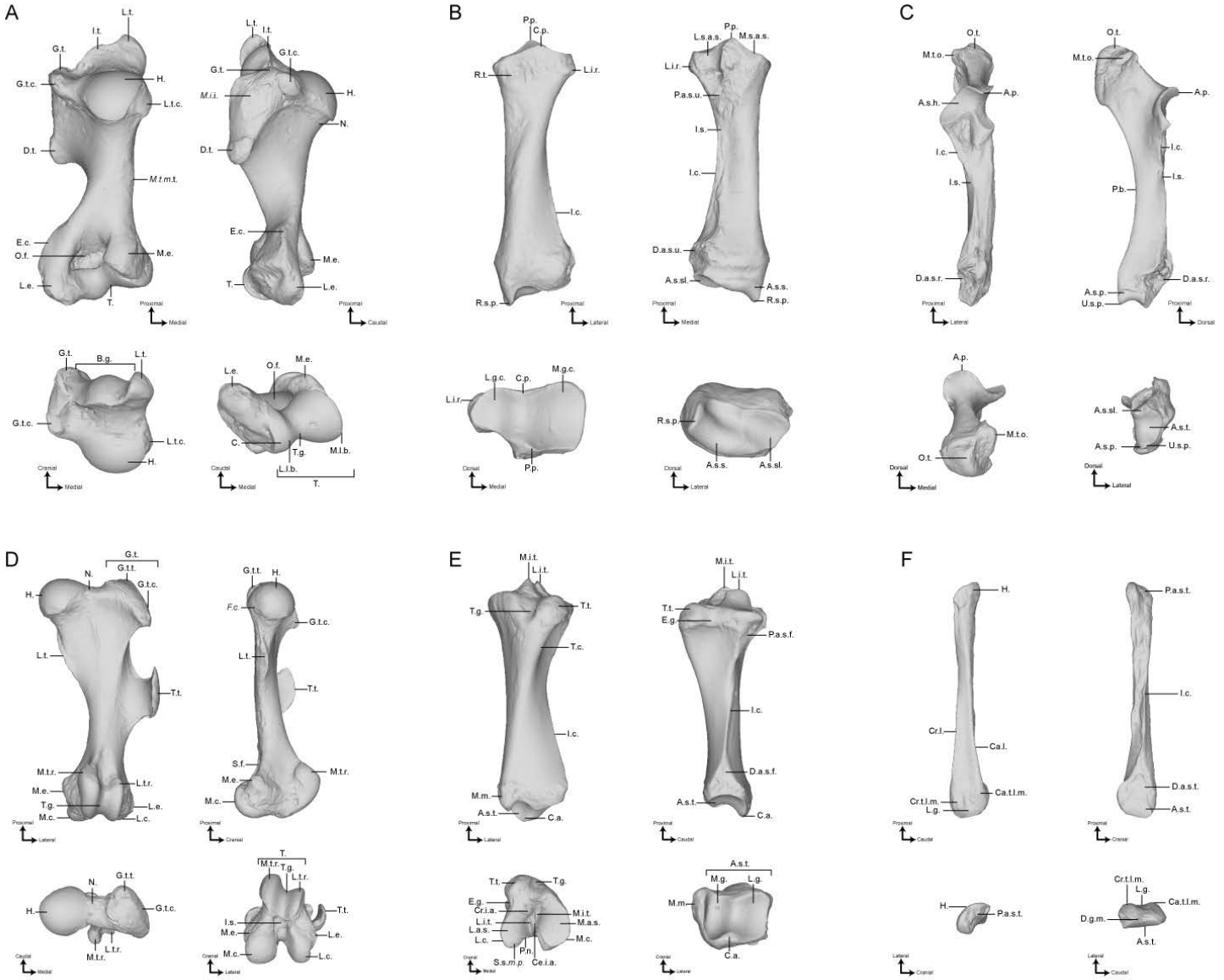
A
L.t.
I.t.
G.t.
G.t.c.
H.
L.t.c.
D.t.
M.t.m.t.
E.c.
O.f.
M.e.
L.e.
T.
Proximal
Medial
G.t.c.
M.i.i.
N.
Caudal
B.g.
C.
T.g.
M.l.b.
L.l.b.
Cranial
B
Pp.
C.p.
R.t.
L.i.r.
I.c.
R.s.p.
L.s.a.s.
M.s.a.s.
P.a.s.u.
I.s.
D.a.s.u.
A.s.sl.
A.s.s.
L.g.c.
M.g.c.
Dorsal
Lateral
C
O.t.
M.t.o.
A.p.
A.s.h.
D.a.s.r.
P.b.
A.s.p.
U.s.p.
D
F.c.
S.f.
M.t.r.
M.c.
L.c.
L.t.r.
T.g.
M.e.
L.e.
E
M.i.t.
L.i.t.
T.t.
T.g.
T.c.
M.m.
A.s.t.
C.a.
E.g.
P.a.s.f.
D.a.s.f.
Cr.i.a.
L.a.s.
P.h.
S.s.m.p.
Ce.i.a.
M.g.
F
Cr.l.
Ca.l.
Cr.t.l.m.
L.g.
Ca.t.l.m.
D.g.m.

963

Data S2: Designation and location of the anatomical landmarks placed on each bone.

Bone	Anatomical LM	Curve sliding semi-LM	Surface sliding semi-LM	Total
Humerus	35	639	559	1233
Radius	23	393	493	909
Ulna	21	343	540	904
Femur	27	612	518	1157
Tibia	24	384	540	948
Fibula	12	269	454	735

Table S2A: Total number of anatomical landmarks (LM), curve sliding and surface sliding semi-landmarks for each bone.

LM	Designation
1	Most distal point of the lateral border of the bicipital groove
2	Most proximal point of the lateral border of the bicipital groove
3	Most proximal point of the intermediate tubercle
4	Most proximal point of the medial border of the bicipital groove
5	Most distal point of the medial border of the bicipital groove
6	Most distal point of the intermediate tubercle
7	Most medial point of the top of the lesser tubercle
8	Most cranial point of the lesser tubercle convexity
9	Most medio-caudal point of the lesser tubercle convexity
10	Most medial point of the humeral head surface
11	Most caudo-distal point of the humeral head surface
12	Contact point between the tricipital line and the caudal border of the articular head surface
13	Most lateral point of the humeral head surface
14	Most caudal point of the greater tubercle convexity
15	Most proximal point of the greater tubercle convexity
16	Most cranial point of the greater tubercle convexity crest
17	Most proximal point of the m. infraspinatus lateral insertion
18	Most distal point of the m. infraspinatus lateral insertion
19	Most proximal point of the deltoid tuberosity
20	Most distal point of the deltoid tuberosity
21	Most proximal point of the epicondylar crest tuberosity
22	Most distal point of the epicondylar crest tuberosity
23	Most lateral point of the lateral epicondyle
24	Most distal point of the lateral epicondyle
25	Most proximo-lateral point of the capitulum
26	Most cranio-proximal point of contact between the trochlea and the capitulum
27	Most cranial point of the trochlea groove
28	Most cranio-medial point of the dorsal side of the trochlea
29	Most distal contact point between the trochlea border and the medial development of the trochlea lip
30	Most cranio-medial point of the ventral side of the trochlea
31	Most cranio-lateral point of the ventral side of the trochlea
32	Most caudo-distal point of contact between the capitulum and the trochlea
33	Most medial point of the medial epicondyle
34	Most caudal point of the medial epicondyle
35	Most lateral point of the medial epicondyle

970

971 **Table S2B:** Designation of the anatomical landmarks on the humerus.

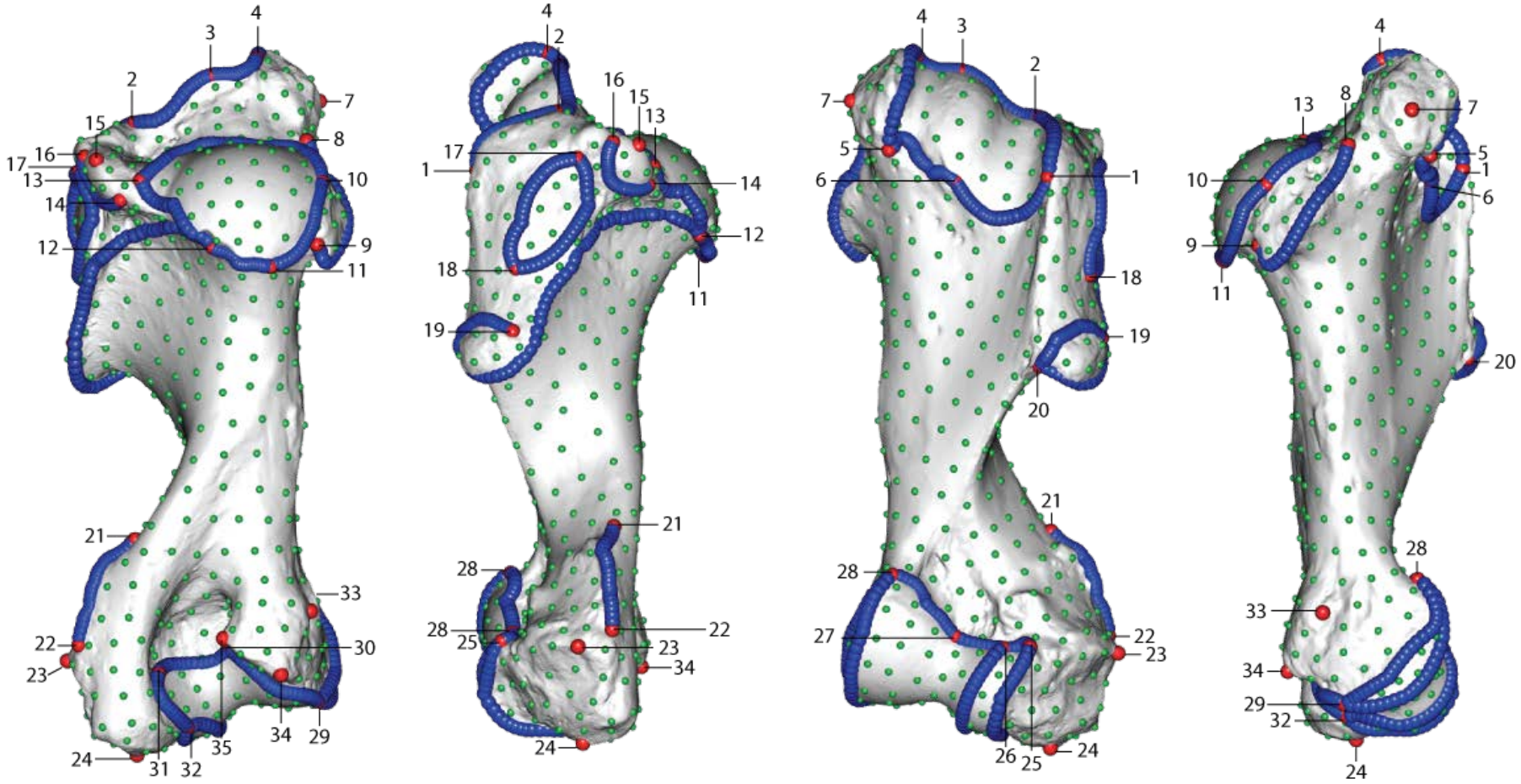

Figure S2C: Location of the anatomical landmarks (red spheres), curve sliding (blue spheres) and surface sliding (green spheres) semi-landmarks placed on the humerus. From left to right: caudal, lateral, cranial and medial views. Numbers refer to anatomical landmarks designation detailed in Table S1B.

LM	Designation
1	Most caudo-lateral point of the lateral glenoid cavity
2	Most cranio-lateral point of the lateral glenoid cavity
3	Tip of the coronoid process
4	Most cranial point of the medial glenoid cavity
5	Most caudo-medial point of the medial glenoid cavity
6	Tip of the palmar process of the glenoid cavity ridge
7	Most cranial point of the lateral insertion relief
8	Most lateral point of the lateral insertion relief
9	Most caudo-distal point of the proximo-lateral articular facet for the ulna
10	Most caudo-distal point of the proximo-medial articular facet for the ulna
11	Most proximal point of the interosseous crest (= most distal point of the interosseous space)
12	Most distal point of the interosseous crest (crossing the distal epiphysis line)
13	Most cranio-lateral point of the disto-lateral articulation surface for ulna
14	Most proximo-lateral point of the disto-lateral articulation surface for ulna
15	Most caudo-lateral point of the disto-lateral articulation surface for ulna
16	Most medial point of the transversal crest
17	Tip of the radial styloid process
18	Maximum of curvature of the cranial ridge of the articular facet for the scaphoid
19	Most cranio-lateral point of the articular facet for the scaphoid
20	Most lateral point of the articular facet for the semilunar
21	Most caudo-lateral point of the articular facet for the semilunar
22	Most caudo-lateral point of the articular facet for the scaphoid
23	Most cranio-proximal point of the medial facet of distal radius

Table S2D: Designation of the anatomical landmarks on the radius.

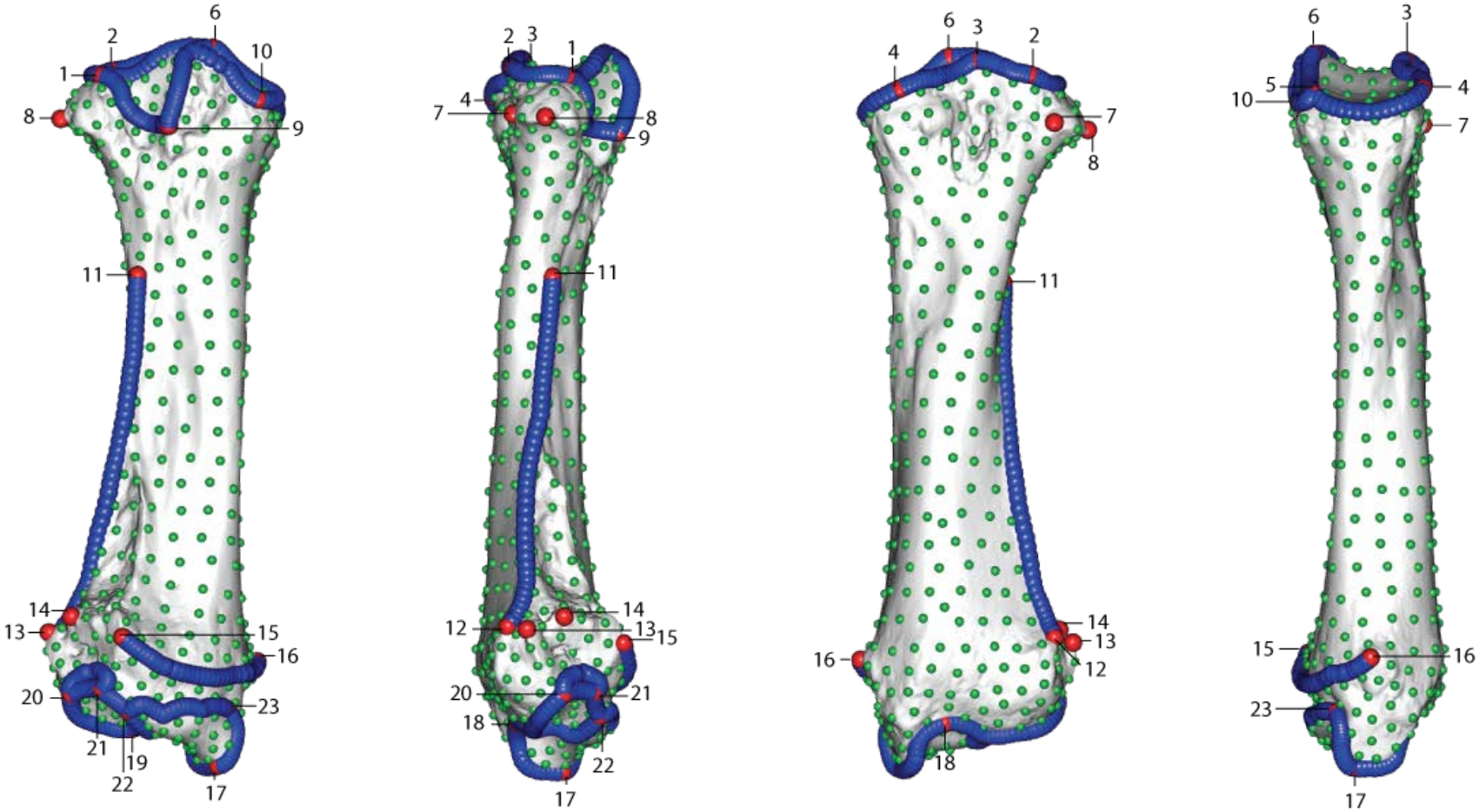

Figure S2E: Location of the anatomical landmarks (red spheres), curve sliding (blue spheres) and surface sliding (green spheres) semi-landmarks placed on the radius. From left to right: caudal, lateral, cranial and medial views. Numbers refer to anatomical landmarks designation detailed in Table S1D.

LM	Designation
1	Most proximo-cranial point of the olecranon tuberosity cranial border
2	Most lateral point of the olecranon tuberosity
3	Most caudo-distal point of the olecranon tuberosity
4	Most medial point of the olecranon tuberosity
5	Most proximal point of the olecranon tuberosity
6	Cranial tip of the anconeal process
7	Most distal point of the lateral part of the trochlear notch articular surface
8	Maximum concavity point of the distal border of the trochlear notch articular surface
9	Most distal point of the medial part of the trochlear notch articular surface
10	Most distal point of the proximo-medial articular facet for the radius
11	Most distal point of the proximo-lateral articular facet for the radius
12	Most distal point of the proximal synostosis surface for the radius (= most proximal point of the interosseous space)
13	Most medio-caudal point of the distal radio-ulnar synostosis surface
14	Most disto-medial point of the articular surface with the semilunar bone
15	Most cranio-lateral point of the articular surface with the semilunar bone
16	Most disto-lateral point of the articular surface with the semilunar bone
17	Most cranio-lateral point of the distal radio-ulnar synostosis surface
18	Most lateral point of the distal epiphysis
19	Caudo-distal tip of ulnar styloid process
20	Most proximal contact point between the articular surfaces for the pisiform and the triquetrum
21	Most distal contact point between the caudal border of the ulna and the articular surface with the pisiform

Table S2F: Designation of the anatomical landmarks on the ulna.

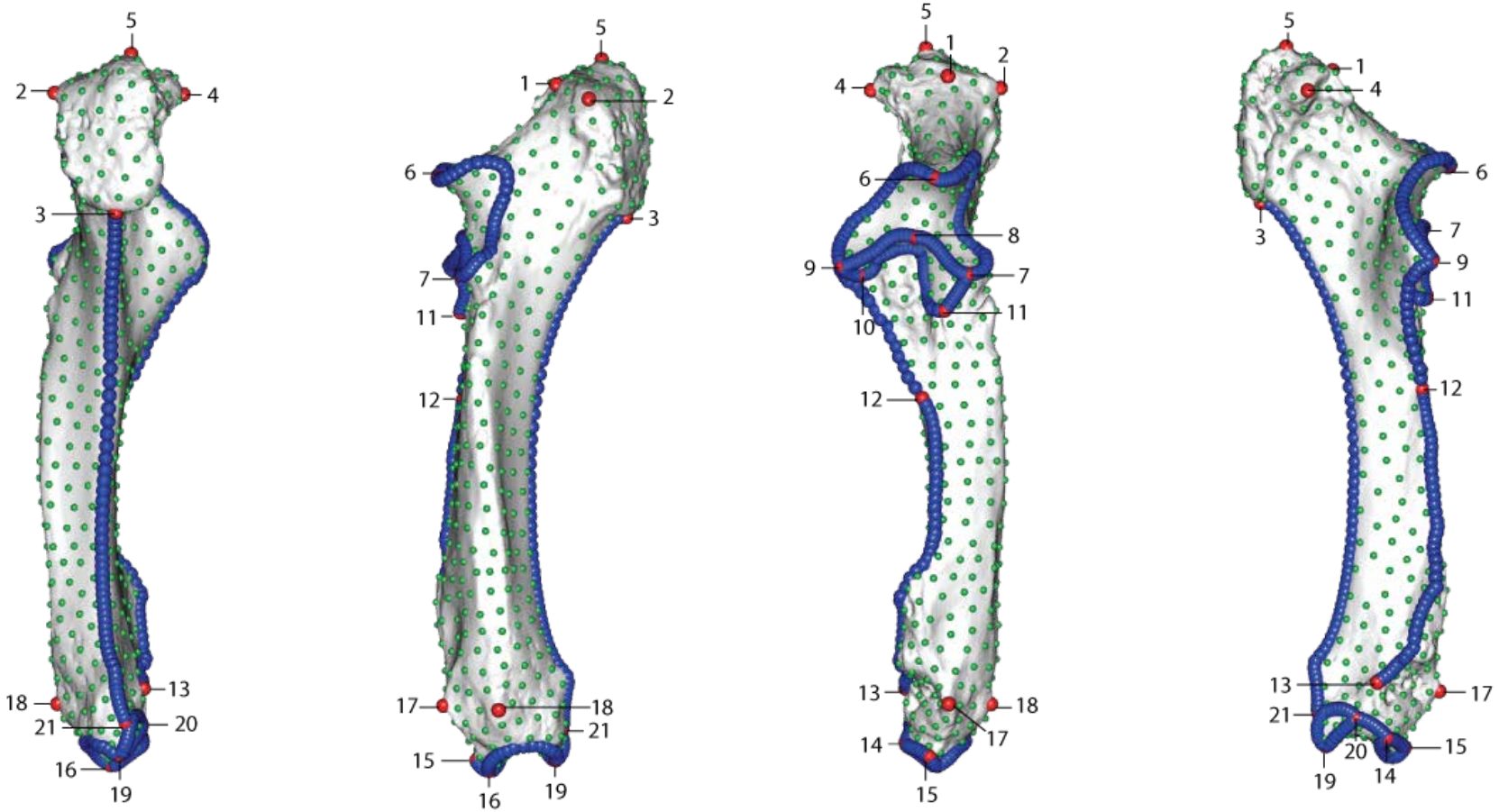

Figure S2G: Location of the anatomical landmarks (red spheres), curve sliding (blue spheres) and surface sliding (green spheres) semi-landmarks placed on the ulna. From left to right: caudal, lateral, cranial and medial views. Numbers refer to anatomical landmarks designation detailed in Table S1F.

LM	Designation
1	Most proximo-cranial point of the greater trochanter
2	Most proximo-caudal point of the greater trochanter
3	Most medial point of the greater trochanter convexity
4	Most distal point of the intertrochanteric crest
5	Most disto-caudal point of the greater trochanter
6	Most cranio-lateral point of the convexity of the greater trochanter
7	Most proximal contact point between the intertrochanteric line and the medial line of the cranial face
8	Most lateral point of the border of the head
9	Most proximal point of the lesser trochanter
10	Most distal point of the lesser trochanter
11	Most proximal point of the gluteal tuberosity on the third trochanter
12	Most distal point of the gluteal tuberosity on the third trochanter
13	Most medial point of the medial epicondyle
14	Contact point between the intercondylar line and the medial condyle
15	Contact point between the intercondylar line and the lateral condyle
16	Most lateral point of the lateral epicondyle
17	Most proximal point of the lateral lip of the trochlea
18	Most proximal point of the trochlear groove
19	Most proximal point of the medial lip of the trochlea
20	Most distal point of the medial lip of the trochlea
21	Distal maximum of curvature of the trochlear groove
22	Most distal point of the lateral lip of the trochlea
23	Most medial point of the fossa extensoria
24	Most lateral point of the fossa extensoria
25	Most cranial point of the fossa extensoria
26	Most proximo-medial point of the lateral condyle articular surface
27	Most proximo-lateral point of the medial condyle articular surface

Table S2H: Designation of the anatomical landmarks on the femur.

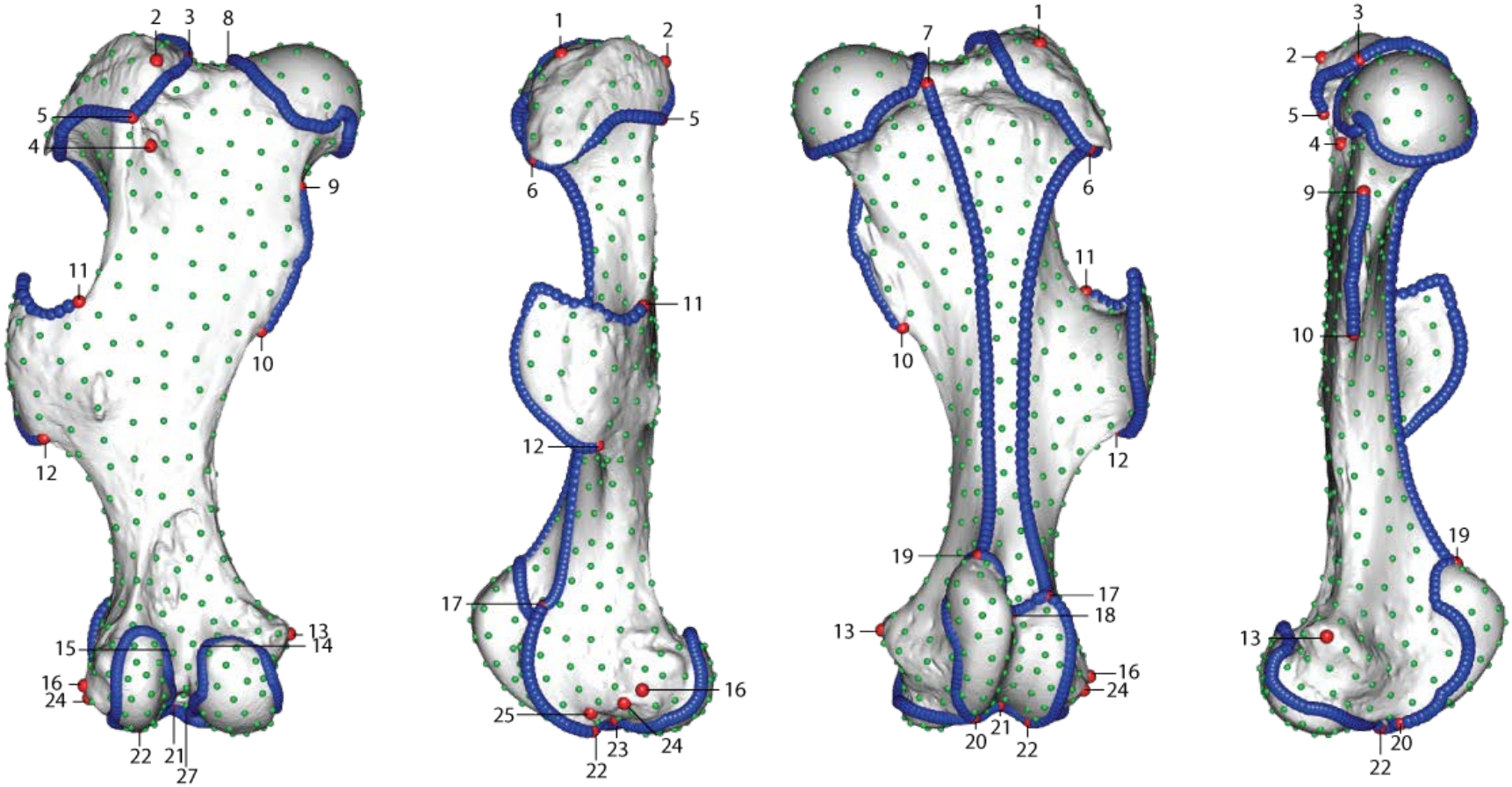

Figure S2I: Location of the anatomical landmarks (red spheres), curve sliding (blue spheres) and surface sliding (green spheres) semi-landmarks placed on the femur. From left to right: caudal, lateral, cranial and medial views. Numbers refer to anatomical landmarks designation detailed in Table S1H. Landmark n°26 situated in the intercondylar space cannot be seen.

LM	Designation
1	Most proximal point of the lateral tubercle of the intercondylar eminence
2	Most proximo-cranial point of the lateral tubercle of the intercondylar eminence
3	Most cranial point of the articular surface of the lateral condyle
4	Most caudal point of the articular surface of the lateral condyle
5	Most caudal point of the lateral tubercle of the intercondylar eminence
6	Most caudo-proximal point of the medial tubercle of the intercondylar eminence
7	Most proximal point of the medial tubercle of the intercondylar eminence
8	Most cranial point of the articular surface of the medial condyle
9	Most caudal point of the articular surface of the medial condyle
10	Most proximal point of the proximal tibio-fibular synostosis surface
11	Most distal point of the proximal tibio-fibular synostosis surface
12	Most proximal point of the lateral part of the tibial tuberosity
13	Most distal point of the lateral part of the tibial tuberosity
14	Most distal point of the tibial tuberosity groove
15	Most proximal point of the medial part of the tibial tuberosity
16	Most caudal point of the medial condyle
17	Most proximal point of the distal tibio-fibular synostosis surface
18	Most caudo-lateral point of the distal articular surface
19	Most cranio-lateral point of the distal articular surface
20	Most cranio-distal point of the intermediate ridge of the distal articular surface
21	Most distal point of the contact between the medial malleolus and the distal articular surface
22	Most distal point of the medial part of the distal articular surface
23	Most caudo-distal point of the intermediate ridge of the distal articular surface
24	Most medial point of the medial malleolus

Table S2J: Designation of the anatomical landmarks on the tibia.

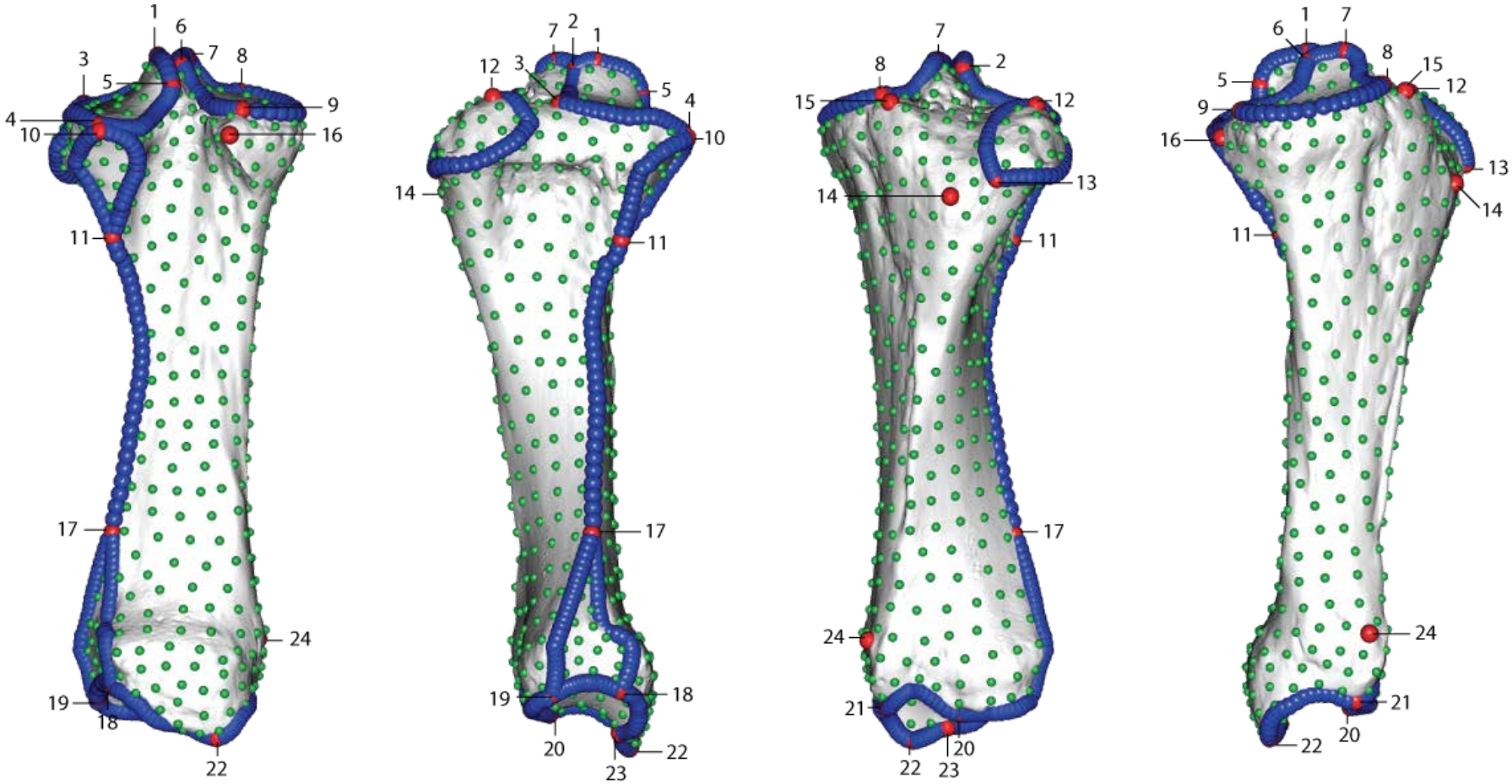

Figure S2K: Location of the anatomical landmarks (red spheres), curve sliding (blue spheres) and surface sliding (green spheres) semi-landmarks placed on the tibia. From left to right: caudal, lateral, cranial and medial views. Numbers refer to anatomical landmarks designation detailed in Table S1J.

LM	Designation
1	Most proximal point of the proximal tibio-fibular synostosis surface
2	Most caudo-medial point of the proximal tibio-fibular synostosis surface
3	Most cranio-lateral point of the proximal tibio-fibular synostosis surface
4	Most proximal point of the distal tibio-fibular synostosis surface
5	Most caudal point of the distal articular facet
6	Most distal point of the caudal part of the distal articular facet
7	Most distal point of the cranial part of the distal articular facet
8	Most cranial point of the distal articular facet
9	Distal tip of the caudal ridge of the lateral malleolar sulcus
10	Distal tip of the cranial ridge of the lateral malleolar sulcus
11	Most lateral point of the cranial ridge of the lateral malleolar sulcus
12	Most disto-medial point of the proximal epiphysis = end of the latero-caudal crest

0 **Table S2L:** Designation of the anatomical landmarks on the fibula.

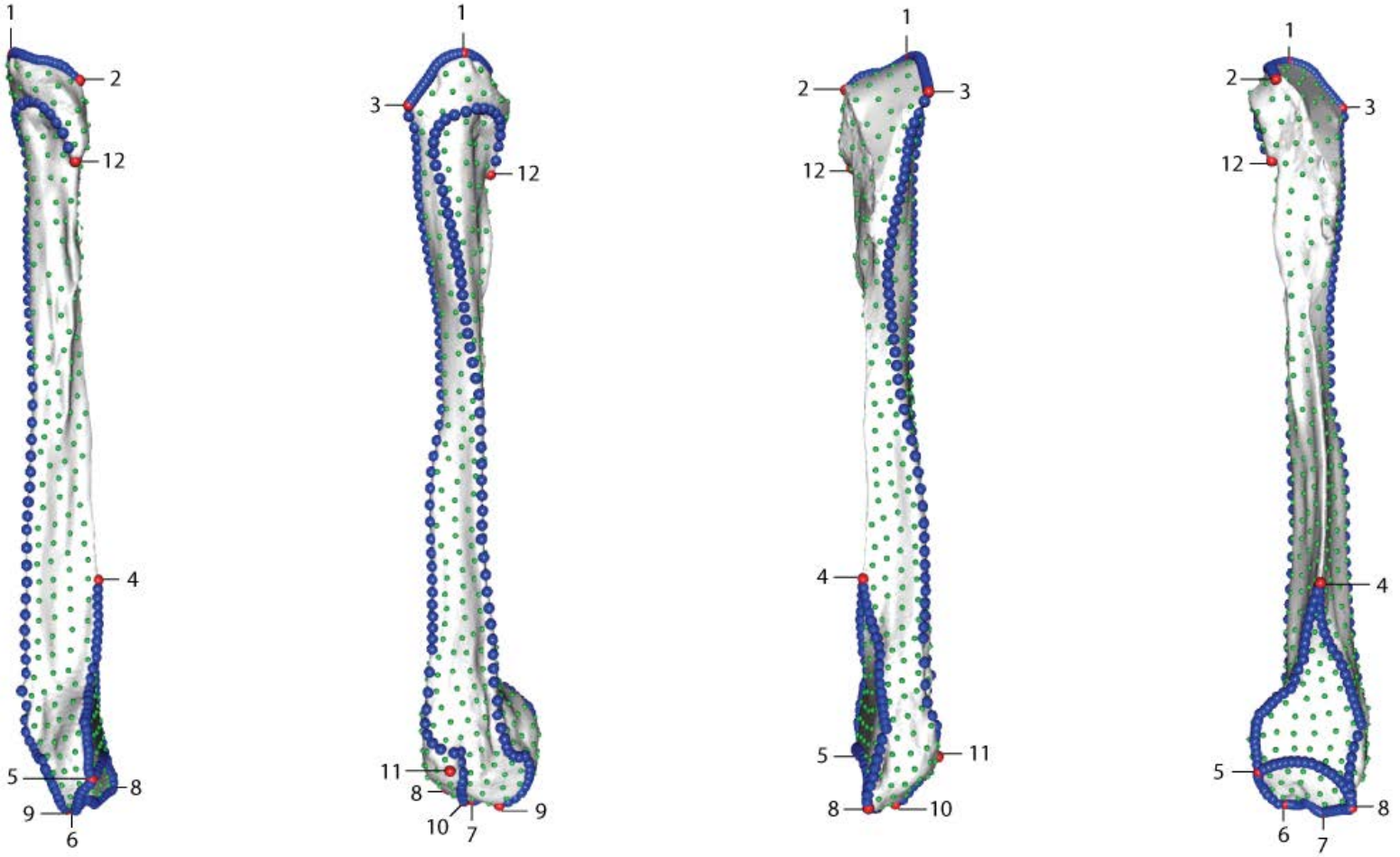

Figure S2M: Location of the anatomical landmarks (red spheres), curve sliding (blue spheres) and surface sliding (green spheres) semi-landmarks placed on the fibula. From left to right: caudal, lateral, cranial and medial views. Numbers refer to anatomical landmarks designation detailed in Table S1L.

Figure S3: Plots of the second PLS axes computed on raw shapes. A: humerus-radius; B: humerus-ulna; C: humerus-femur; D: humerus-tibia; E: humerus-fibula; F: radius-ulna; G: radius-femur; H: radius-tibia; I: radius-fibula; J: ulna-femur; K: ulna-tibia; L: ulna-fibula; M: femur-tibia; N: femur-fibula; O: tibia-fibula. rPLS: value of the PLS coefficient; % EC: percentage of explained covariation; Corr. p-value: corrected p-value using a Benjamini-Hochberg correction.

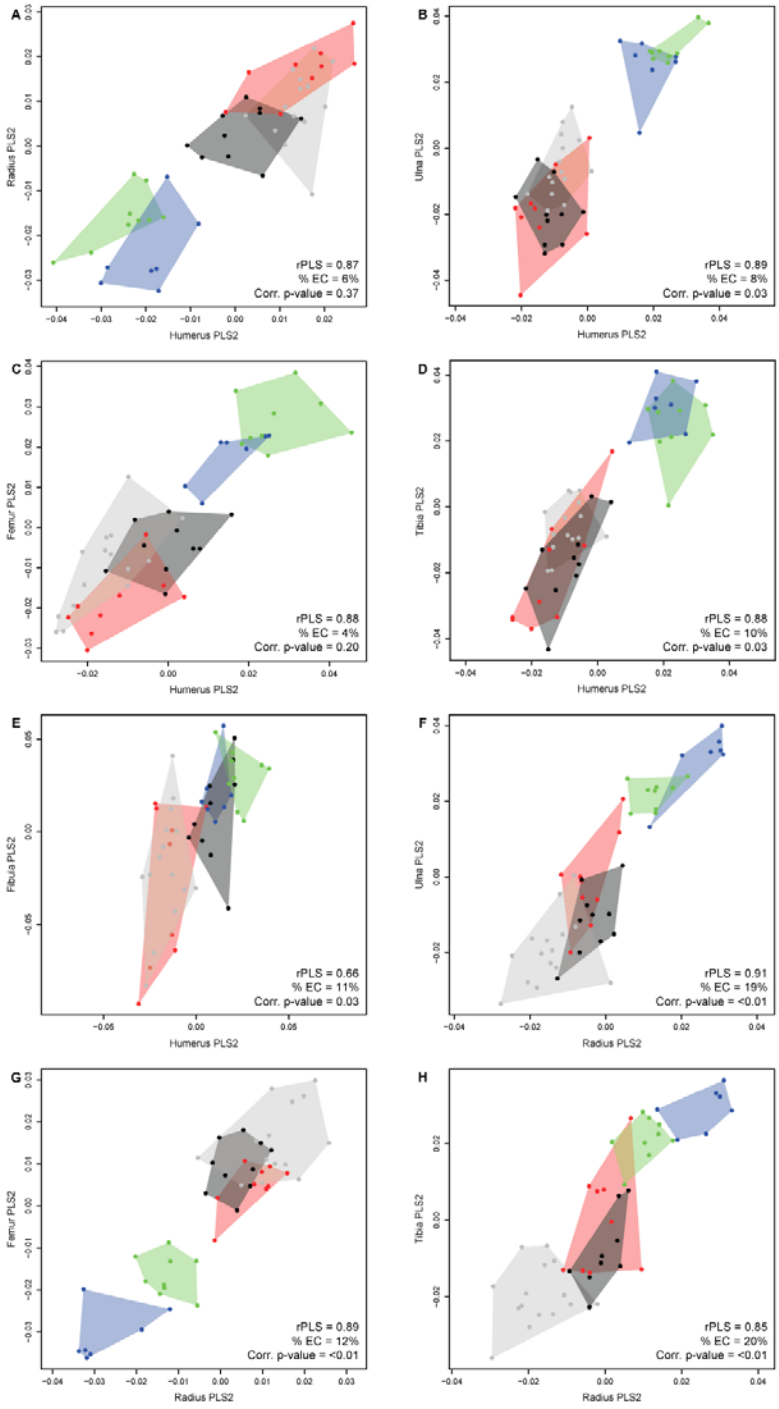

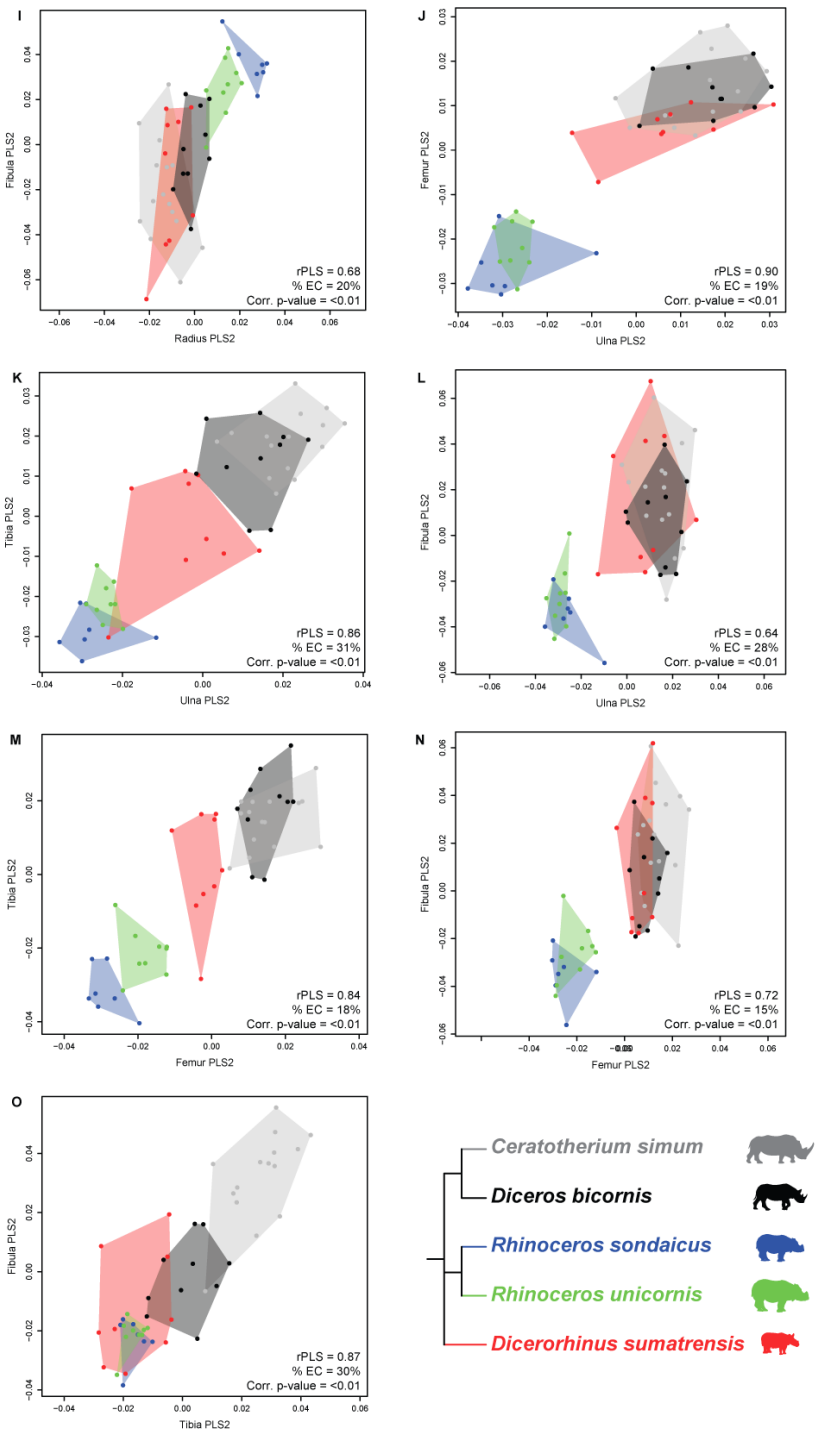
I
Fibula PLS2
Radius PLS2
rPLS = 0.68
% EC = 20%
Corr. p-value = <0.01
J
Femur PLS2
Ulna PLS2
rPLS = 0.90
% EC = 19%
Corr. p-value = <0.01
K
Tibia PLS2
Ulna PLS2
rPLS = 0.86
% EC = 31%
Corr. p-value = <0.01
L
Fibula PLS2
Ulna PLS2
rPLS = 0.64
% EC = 28%
Corr. p-value = <0.01
M
Tibia PLS2
Femur PLS2
rPLS = 0.84
% EC = 18%
Corr. p-value = <0.01
N
Fibula PLS2
Femur PLS2
rPLS = 0.72
% EC = 15%
Corr. p-value = <0.01
O
Fibula PLS2
Tibia PLS2
rPLS = 0.87
% EC = 30%
Corr. p-value = <0.01
Ceratotherium simum
Diceros bicornis
Rhinoceros sondaicus
Rhinoceros unicornis
Dicerorhinus sumatrensis

10

Figure S4: Shape deformations associated with the first PLS axes for the fifteen bone pairs. Blue: negative side of the axis. Orange: positive side of the axis. The colour code of the squares expresses the type of relation between bones as described in the Figure 1 (black: intra-limb relation; orange: serial homology; blue: functional analogy; green: non-homologous or analogous bones). A: humerus-radius; B: humerus-ulna; C: radius-ulna; D: femur-tibia; E: femur-fibula; F: tibia-fibula; G: humerus-femur; H: radius-tibia; I: radius-fibula; J: ulna-tibia; K: ulna-fibula; L: humerus-tibia; M: humerus-fibula; N: radius-femur; O: ulna-femur.

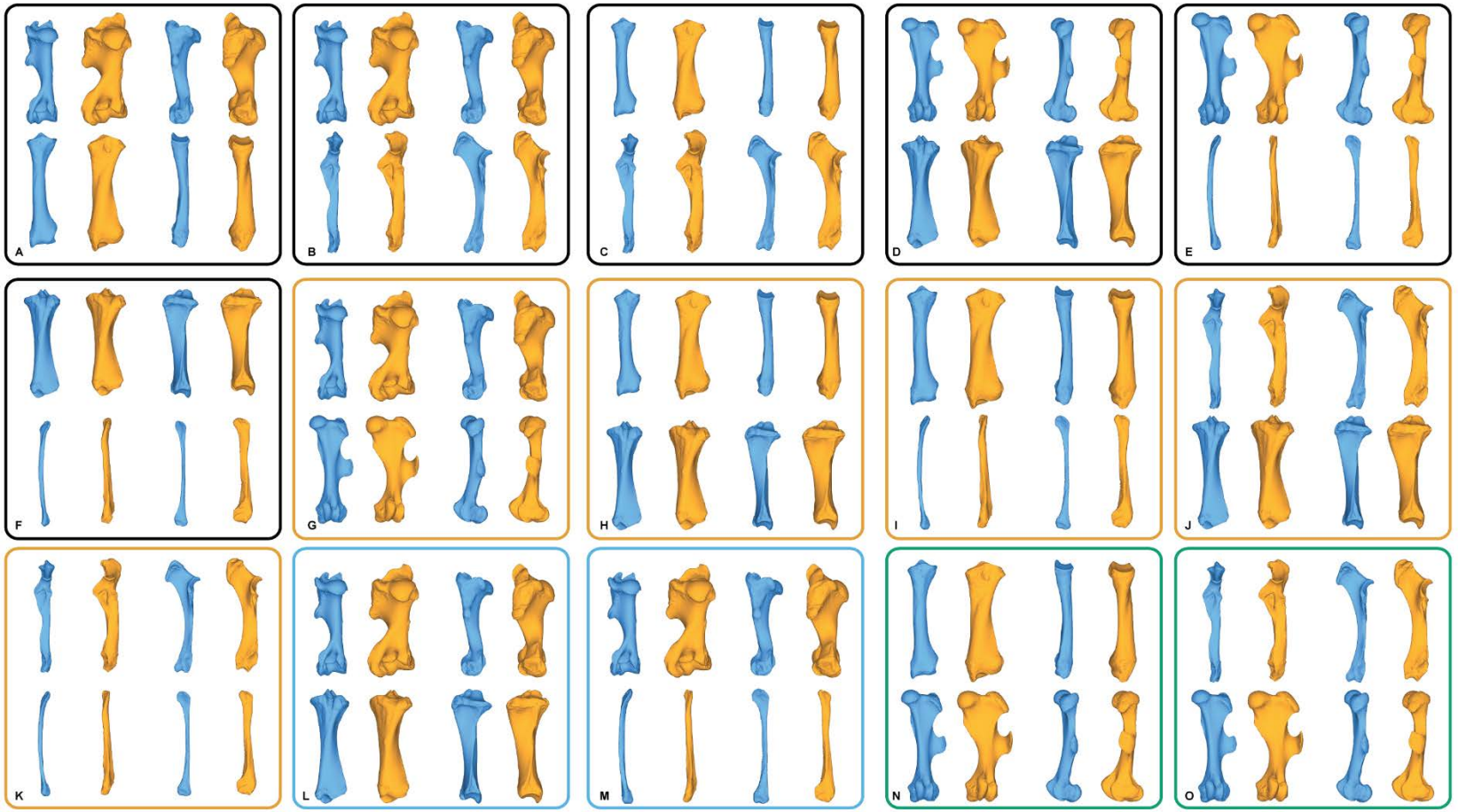

Figure S5: Colour maps of the location and intensity of the shape deformation associated to the first PLS axes for 4 pairs of bones among the five species of rhinoceros. For each bone, the shape associated to the positive part of the first PLS axis was coloured depending on its distance to the shape associated to the negative part (blue indicates a low deformation intensity and red indicate a high deformation intensity). The colour code of the squares expresses the type of relation between bones as described in the Figure 1 (black: intra-limb relation; orange: serial homology; blue: functional analogy; green: non-homologous or analogous bones). A: humerus-radius; B: humerus-ulna; C: femur-fibula; D: radius-fibula; E: ulna-tibia; F: humerus-fibula; G: radius-femur (orientation from left to right in each case: cranial, lateral, caudal and medial).

27

28

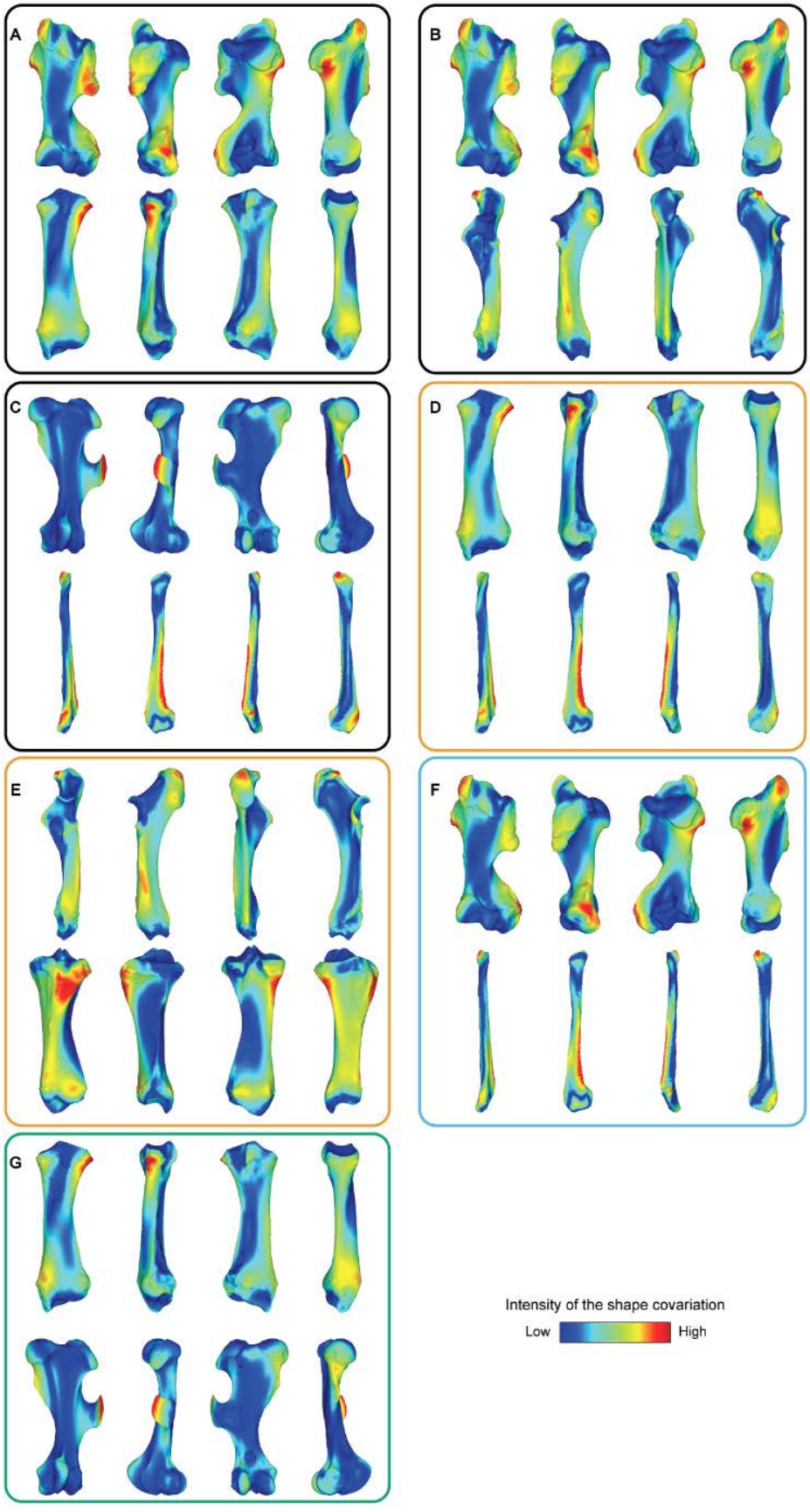

Figure S6: Shape deformations associated with the first PLS axes for the fifteen bone pairs. Blue: negative side of the axis. Orange: positive side of the axis. The colour code of the squares expresses the type of relation between bones as described in the Figure 1 (black: intra-limb relation; orange: serial homology; blue: functional analogy; green: non-homologous or analogous bones). A: humerus-radius; B: humerus-ulna; C: radius-ulna; D: femur-tibia; E: femur-fibula; F: tibia-fibula; G: humerus-femur; H: radius-tibia; I: radius-fibula; J: ulna-tibia; K: ulna-fibula; L: humerus-tibia; M: humerus-fibula; N: radius-femur; O: ulna-femur.

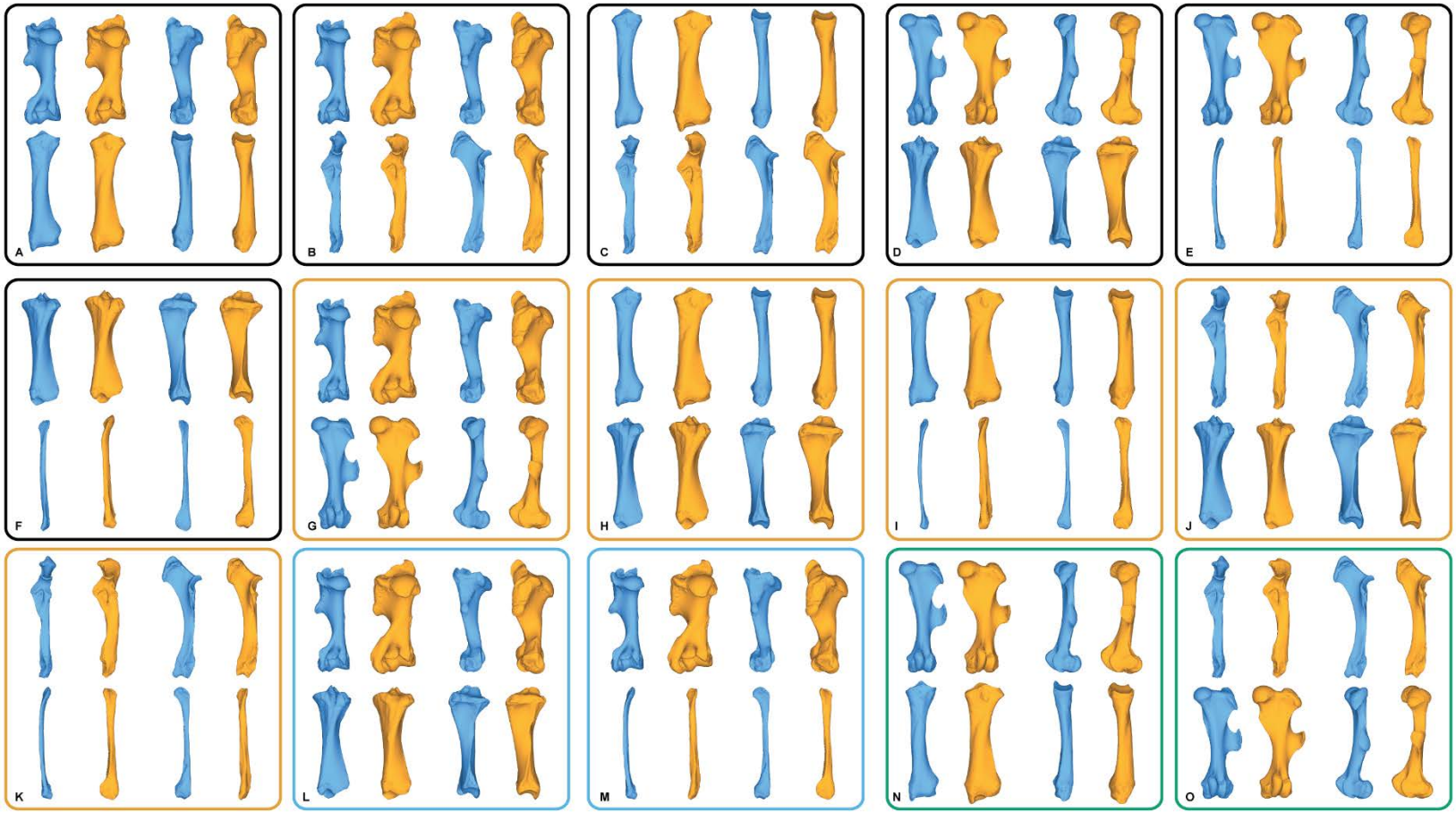

Figure S7: Plots of the first PLS axes computed at the intraspecific level for all the pairs displaying a significant p-value before the Benjamini-Hochberg correction. Abbreviations: A: adult; SA: subadult; M: male; F: female; U: sex unknown.

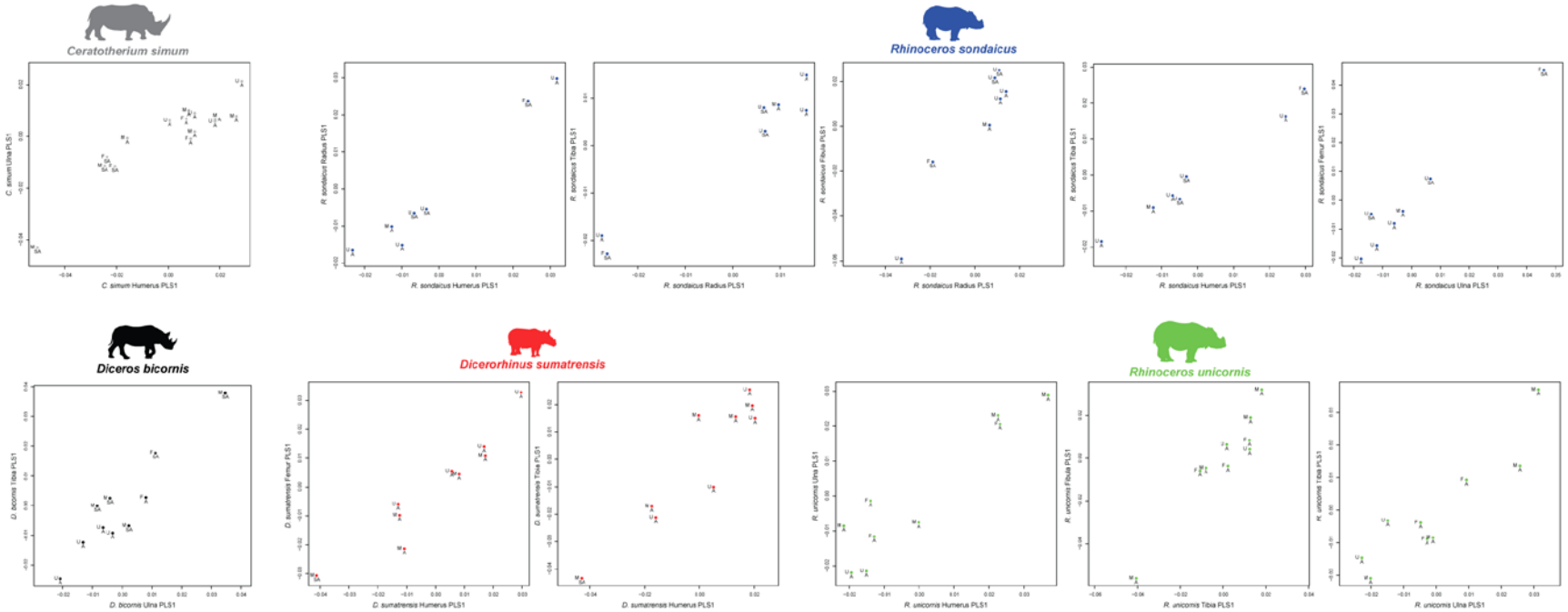

Figure S8: Colour maps of the location and intensity of the shape deformation associated to the first PLS axes for all the pairs displaying a significant p-value before the Benjamini-Hochberg correction. For each bone, the shape associated to the positive part of the first PLS axis was coloured depending on its distance to the shape associated to the negative part (blue indicates a low deformation intensity and red indicate a high deformation intensity). The colour code of the squares expresses the type of relation between bones as described in the Figure 1 (black: intra-limb relation; orange: serial homology; blue: functional analogy; green: non-homologous or analogous bones).

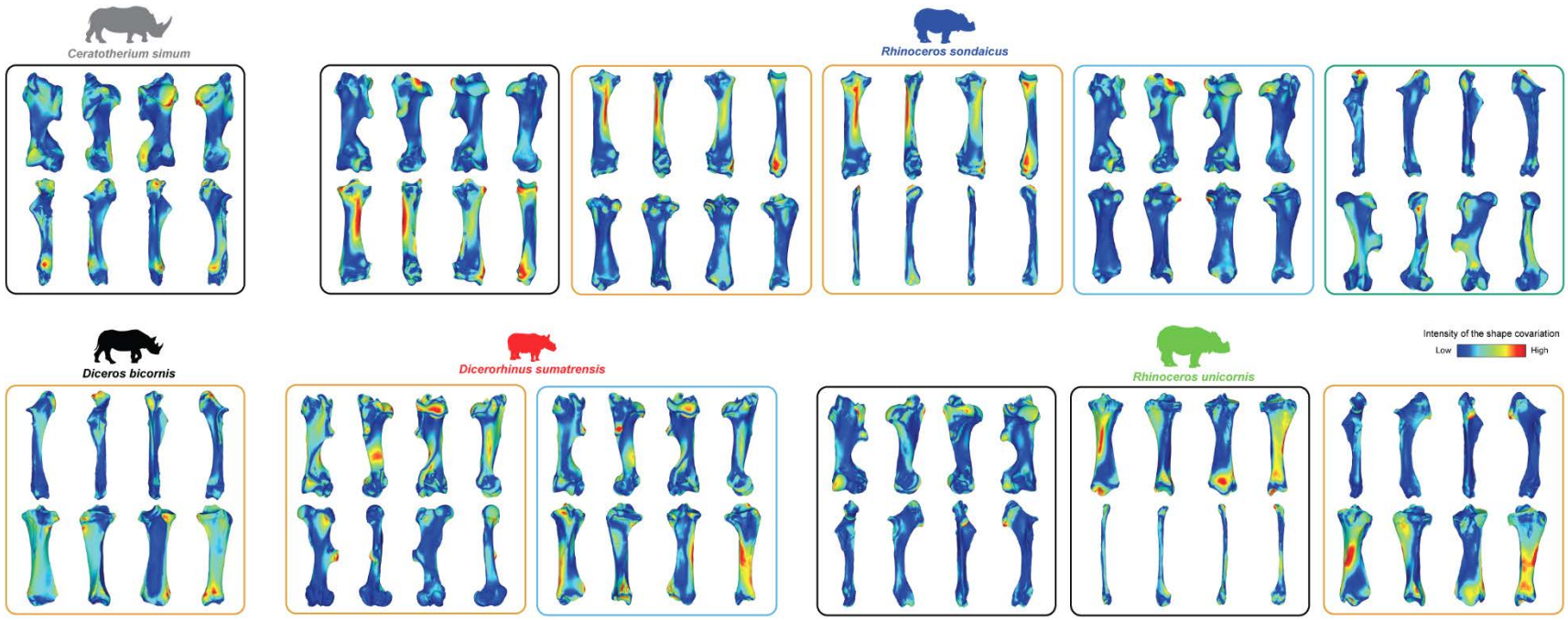

45